This is a repository copy of *A novel smart framework for sustainable nanocomposite electrolytes based on ionic liquids of dye-sensitized solar cells by a covalently multifunctional graphene oxide-vinyl imidazole/4-tert-butylpyridine cobalt complex*.

Article:

A novel smart framework for sustainable nanocomposite electrolytes based on ionic liquids of dye-sensitized solar cells by a covalently multifunctional graphene oxide-vinyl imidazole/4-tert-butylpyridine cobalt complex (Experiments, Artificial intelligence, and density functional theory studies)

Mohammad Mohammadizadeh Boghrabad[a], Elaheh Kowsari[a,*], Seeram Ramakrishna[b,*], Saeedeh Sarabadani Tafreshi[a], Mahsa Gholambargani [c], Mahboobeh Rafieepoor Chirani[a], Shiva Orangi[a], Mohammad Gheibi [d], Majid Abdouss[a], Amutha Chinnappan[b], Nora H. de Leeuw[e,f]

[a] Department of Chemistry, Amirkabir University of Technology, No. 424, Hafez Avenue, 1591634311, Tehran, Iran

[b] Department of Mechanical Engineering, Center for Nanofibers and Nanotechnology, National University of Singapore, 119260, Singapore

[c] Nanotechnology and Advanced Materials Department, Materials and Energy Research Center (MERC), Karaj, Iran

[d] Department of Civil Engineering, Ferdowsi University of Mashhad, Mashhad, Iran

[e] School of Chemistry, Cardiff University, Main Building, Park Place, Cardiff CF10 3AT, United Kingdom

[f] School of Chemistry, University of Leeds, Leeds LS2 9JT, United Kingdom[1]

Abstract

In this study, covalently multifunctional graphene oxide (GO) with vinyl imidazole/4-tert-butylpyridine cobalt complex (GO-VI/TBP cobalt complex) was synthesized through a novel approach. To this end, GO was functionalized with 1-vinyl imidazole (VI), followed by establishing a reaction between GO-VI, 4-tert-butylpyridine (TBP), and anhydrous $CoCl_2$. Then, in dye-sensitized solar cells (DSSCs), this synthesized compound was used as an effective additive in sustainable nanocomposite electrolytes based on 1-butyl-3-methylimidazolium iodide (BMII)

* Corresponding authors.
  E-mail addresses: Kowsarie@aut.ac.ir (E. Kowsari), seeram@nus.edu.sg (S. Ramakrishna)

[1] Present address.

and 1-ethyl-3-methylimidazolium iodide (EMII) ionic liquids (ILs). Adding 0.6 wt.% of optimal GO-VI/TBP cobalt complex to electrolyte increased the conversion efficiency of DSSCs significantly up to 7.359% compared to 4.130% in the initial standard DSSCs. This 78.18% efficiency increase demonstrates how the GO-VI/TBP cobalt complex as a molecular bridge affects the conductivity and electron transport in the electrolyte based on ionic liquids. By enhancing the I^-/I_3^- diffusion coefficient, cobalt complexes with the TBP ligand and nitrogen-containing heterocyclic compounds in GO-VI/TBP cobalt complex compounds accelerated electron transfers and ion conductivity in the electrolyte. As a result, the short circuit current density (Jsc) increased from 8.131 to 14.301 mA cm^{-2}, and the open-circuit voltage (V_{OC}) rose from 0.725 to 0.754 V. Density functional theory (DFT) studies showed an increase in the conduction band of the TiO_2 electrode after the adsorption of the electrolyte additives on its surface. This upward shift resulted in the quick injection of electrons from the dye's lowest unoccupied molecular orbital (LUMO) to the TiO_2 electrode's conduction band. Finally, a soft computing system was designed to predict experimental features (V_{OC} and J_{SC}) based on effective factors. Based on the results, Random Tree, Random Forest, and Multilayer Perceptron (MLP) methods with correlation coefficients greater than 0.92 have the highest efficiency for creating the soft sensor. Overall, this work can be employed as a novel strategy for advancing the usage of graphene derivatives in this sector to boost the performance of electrolytes.

1. Introduction

Silicon has several applications in most solar cells regarding its great stability and energy conversion efficiency. Today, numerous studies are underway on new generations of solar cells to minimize the cost of synthesis and their usage in the future. Because of their excellent efficiency and features, dye-sensitized solar cells (DSSCs) have been investigated in numerous studies [1-4]. Recently, it has been feasible to achieve photovoltaic conversion efficiency of more than 15% in this type of solar cells owing to research and development on various DSSC components [5]. Sustainability aspects of DSSCs have always been considered in these works. In this regard, several efforts have been made to enhance the efficiency of these cells by synthesizing green and cost-effective ingredients and using these materials in the fabrication of DSSCs. DSSCs are also considered regarding their unique manufacturing and commercial capabilities. The long-run performance of DSSCs is affected by electrolyte leakage when using organic solvent-based electrolytes [6]. In this regard, room temperature ionic liquids (ILs), particularly ILs based on imidazolium cations, are employed in DSSCs to create green and sustainable electrolytes that serve as both iodine sources and electrolyte solvents [7-9]. Chemical and thermal stability, environmental friendliness, the low vapor pressure at room temperature, strong ionic conductivity, tunable viscosity, and negligible electrolyte leakage distinguish ILs-based electrolytes as superior and more acceptable alternatives to organic solvent-based electrolytes [10-12]. Along with ILs, carbon-based materials can improve the conversion efficiency of these electrolytes when incorporating them into the structure of these electrolytes [13, 14]. Owing to their specific characteristics, graphene and its derivatives are among the ideal carbon-based materials for usage in DSSCs to improve the performance of ILs-based electrolytes. In general, adding graphene and its derivatives to ILs-based electrolytes improves the short circuit current density (Jsc), thereby

enhancing the performance of DSSCs [15-17]. The presence of graphene compounds in ILs-based electrolytes can shift and optimize the bandgap of the electrolyte, resulting in improved electron transport from the electrolyte to the anode [18, 19]. Graphene oxide (GO) offers appealing qualities, including environmental friendliness, sustainability, ease of manufacture, and a variety of functional groups with oxygen (e.g., epoxy and hydroxyl groups) [20]. Regarding these qualities, GO can have the potential to be chemically modified. In addition, imidazole compounds can enhance GO's surface and electrical characteristics because of the heterocyclic structure's non-bonding pairs of nitrogen and bonding pairs [13, 21]. In addition, regarding certain capabilities of cobalt in electron transport and the redox pair (I^-/I_3^-), the presence of cobalt compounds in the electrolyte structure can aid oxidation-reduction reaction in the electrolyte [22-25]. Different cobalt oxidation states allow cobalt-containing compounds to be added to the GO structure in the form of complexes and establish distinct cobalt complexes in the functionalized graphene oxide (FGO) structure [26-29]. In this respect, 4-tert-butylpyridine (TBP) can limit the recombination and strengthening of open-circuit voltage (V_{OC}) in the electrolytes of DSSCs. Hence, its use as a ligand in cobalt complexes and its inclusion in the GO structure can make this chemical's role in the electrolyte more striking. [30, 31]. Thus, functionalizing GO with imidazole compounds in one step and then adding cobalt complexes with TBP ligands to its structure can result in a compound that is perfect for use in nanocomposite electrolytes. The explanation is that the imidazole compounds' presence in the compound's structure improves the distribution and mixing of FGO and ILs based on imidazolium cations. Using this FGO as an effective additive and mediator in nanocomposite electrolytes can be a good idea and comparable to other similar studies. The reason is that the presence of cobalt complexes with various ligands enhances the ionic conductivity,

excellent surface characteristics, and performance of the nanocomposite electrolyte in DSSCs by enhancing electron transport [22, 32-34].

The present study describes a unique and creative method for synthesizing a covalently multifunctional GO with vinyl imidazole/4-tert-butylpyridine cobalt complex (GO-VI/TBP cobalt complex) using 1-vinyl imidazole (VI), a low-cost cobalt compound (cobalt(II) chloride hexahydrate), and TBP. This complex is equally as effective as functionalized GOs with cobalt complexes from earlier studies while being more affordable. Studying the effect of cobalt complexes with TBP ligands and imidazole agents in graphene sheets has shown that these complexes improve the characteristics of GO and make it a unique and interesting composition. Therefore, as an effective additive in DSSCs electrolyte, GO-VI/TBP cobalt complex was employed with binary imidazolium-based ILs 1-butyl-3-methylimidazolium iodide (BMII) and 1-ethyl-3-methylimidazolium iodide (EMII). In electrolytes based on BMII and EMII ionic liquids, GO functions as a molecular bridge to accelerate the transfer of ions. In the meantime, the presence of nitrogenous substances and cobalt complexes with TBP ligands in their structure speeds up the exchange processes between I^- and I_3^-. The experimental and computational results from this study demonstrate this research's innovation and intriguing features as well. In the last section of this paper, the machine learning computations, including Random Tree (RT), Random Forest (RF), SMOreg, Multilayer Perceptron (MLP), Gaussian Process (GP), and Meta Bagging (MB), are applied for creating a soft-sensor as an experimental parameter predictor.

2. Experimental

2.1. Materials

Natural graphite powder, Sodium nitrate (NaNO₃), potassium permanganate (KMnO₄), 1-vinyl imidazole (purity > 99%), ethyl iodide (C_2H_5I), butyl iodide (C_4H_9I), 1-methylimidazole and 4-tert-butylpyridine (purity = 98%) were prepared from Sigma-Aldrich Corporation (Milwaukee). Merck supplied sulfuric acid (H_2SO_4), thionyl chloride ($SOCl_2$), cobalt (II) chloride hexahydrate, hydrogen peroxide (H_2O_2), iodine (I_2), lithium iodide (LiI), hydrochloric acid (HCl), and ethanol (Darmstadt, Germany). Moreover, all chemicals and solvents employed in this research were of analytical grade.

2.2. Synthesis of ionic liquids

BMII was synthesized in a 500 mL three-neck round bottom flask fitted with a reflux condenser and a N₂ inlet. First, 1-methylimidazole (1mmol) was charged to the balloon, in an ice water bath. Then, slowly poured butyl iodide (1.5 mmol) and stirred under N₂. In the next step, the reaction solution was stirred for 48 h at 80 ℃. After the reaction is finished and the mixture is cooled down to room temperature, a sticky orange liquid form. This liquid can be purified in multiple steps to yield the IL BMII. The EMII was synthesized similarly and under the same conditions [26, 35]. The products have the following spectral properties: (Bruker advance 300 MHz NMR spectrometer, Germany), BMII; ^{1}H NMR (300 MHz, CDCl₃) δ: 0.92 (t, *J*=7.3 Hz, 3H) 1.30 (sextet, *J*=7.3 Hz, 2H) 1.70 (quintet, *J*=7.3 Hz. 2H) 3.90 (s, 3H), 4.10 (t, *J*=7.3 Hz, 2H) 7.62 (s, 1H) 7.70 (s, 1H) 9.2 (s, 1H); ^{13}C NMR (75 MHz, CDCl₃) δ: 14.0, 19.5, 32.0, 36.6, 45.2,122.9, 124.3, 137.2; FTIR (neat film/NaCl plate) cm⁻¹: 3170, 3020, 2960, 2940, 2878, 1570, 1166, 830.

EMII; ^{1}H NMR (300 MHz, CDCl₃) δ: 1.60 (t, *J*=7.0 Hz, 3H) 3.80 (s, 3H), 3.98 (quartet, *J*=7.0 Hz, 3 H), 7.62 (s, 1H) 7.70 (s, 1H) 9.2 (s, 1H); ^{13}C NMR (75 MHz, CDCl₃) δ: 15.0, 37.01, 41.8, 122.8, 124.9, 137.6. FTIR (500–4000 cm⁻¹, neat film/NaCl plate) cm⁻¹: 3150, 3090, 2980, 2920, 2860, 1575, 1160, 845.

2.3. Synthesis of GO and GO-VI/TBP cobalt complex

We synthesized GO using the natural graphite according to the modified Homer method [36] by adding 1.5 g NaNO₃ and 2 g graphite to 6.75 mL of H_2SO_4. Next, the reaction ingredients were agitated in an ice bath. Afterward, 9 g of KMnO₄ was gently added to the test dish for 1 h. The reaction was agitated in an ice bath at 20°C for 5 days after adding all of the KMnO₄. A thick liquid

was formed after this time. Subsequently, 200 mL of H_2SO_4 (a 30 wt.% aqueous solution) was poured stepwise to the viscous liquid for 1 h, followed by 2 h of stirring. The surplus $MnO_2/KMnO_4$ was then reduced by adding 6 mL of H_2O_2 (a 30 wt.% aqueous solution) to the mixture and agitating it for 2 h. The residue was cleaned 15 times using an H_2SO_4/H_2O_2 solution (each period lasted 1 day). The resultant suspension was repeatedly rinsed in deionized water and filtered by filtration to purify it further and eliminate excess salts and acids. Finally, the synthesized GO was oven-dried in a vacuum at 50°C for 24 h.

We synthesized a functionalized GO with cobalt complexes by forming a covalent bond with 1-vinyl imidazole and then forming a dative bond between the TBP cobalt complexes. To synthesize GO-VI/TBP cobalt complex (FGO with cobalt complexes), the GO was first reacted with $SOCl_2$ at 40°C in a balloon linked to the condenser fitted with a magnetic stirrer for 4 h under a nitrogen environment, followed by washing the product and filtering it with dichloromethane to acylate the GO. Next, 4g f acylated GO was reacted with 5g of 1-vinyl imidazole and 20 mL of DMSO in a balloon linked to a condenser fitted with a magnetic stirrer at 80°C for 24 h after acylation. Then, it was filtered and rinsed with dichloromethane to obtain GO-VI (FGO without cobalt complexes). In the final phase, 1.5 g of GO-VI and 1 g of anhydrous $CoCl_2$ were reacted in a balloon linked to the condenser fitted with a magnetic stirrer at 80°C for 70 h with an excess of 4-TBP. GO-VI/TBP cobalt complex was prepared once the reaction procedure was completed and the product was purified. It is noteworthy that hexahydrate $CoCl_2$ was calcined for 10 h at 140°C in the furnace to produce anhydrous $CoCl_2$. Schematic 1 depicts the synthesis of GO and its functionalization with cobalt complexes.
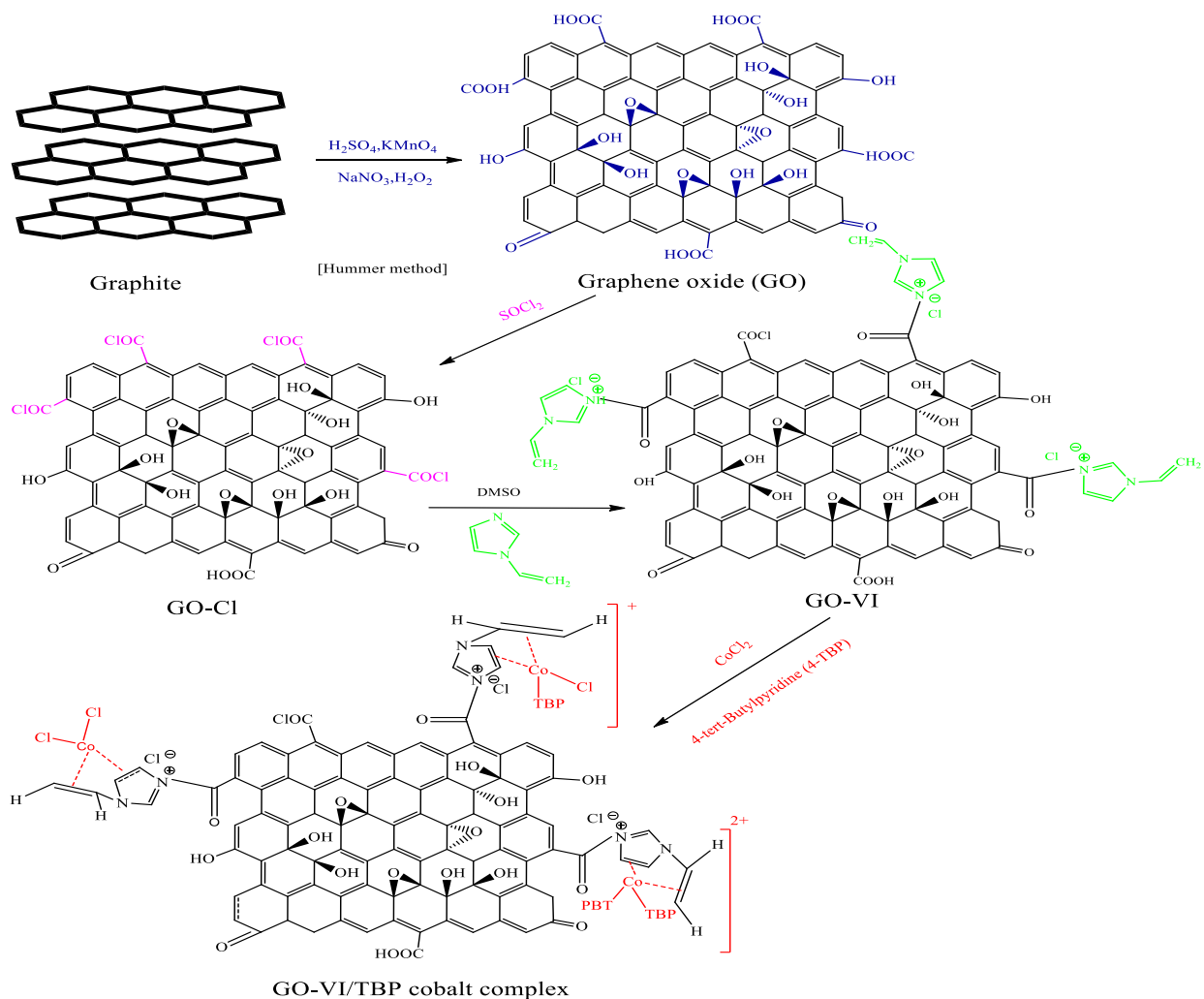
Schematic 1. Steps in the synthesis of GO-VI/TBP cobalt complex

2.4. Preparation of standard and nanocomposite electrolytes

The electrolytes were prepared using a mixture of BMII and EMII ILs in the same amount of 1 M

instead of organic solvents. In a blend of BMII and EMII ILs, 0.1 M LiI, 0.1 M I_2, and 0.5 M TBP

were used to make the standard electrolyte. The nanocomposite electrolytes were made by mixing

the standard electrolyte with optimum concentrations of GO-VI/TBP cobalt complex (0.3, 0.6, and

0.9 wt.%). The nanocomposite electrolytes were then sonicated for 30 min and placed on the

magnetic stirrer for 24 h to evenly distribute the GO-VI/TBP cobalt complex in the IL matrix. The

effect of GO-VI/TBP cobalt complex in nanocomposite electrolytes compared to standard electrolytes was studied after making the nanocomposite electrolytes. Similarly, an electrolyte containing GO-VI additive was prepared to compare with an electrolyte having GO-VI/TBP cobalt complex as an effective additive. Notably, the weight percentage of GO-VI used to prepare the electrolyte was equivalent to the weight percentage of the most effective electrolyte with the GO-VI/TBP cobalt complex as an effective additive.

2.5. Fabrication of DSSCs

The potential contaminations from fluorine-doped tin oxide (FTO) conductive glasses were removed by washing the glasses with water and soap, deionized water, 0.1 M HCl, deionized water, and ethanol, in the order of their appearance. The FTO glasses were heat-treated with a 40 mM $TiCl_4$ aqueous solution for 30 min at 70°C to inhibit photoelectric recombination before being cleaned with ethanol. Afterward, it was rewashed with deionized water and ethanol. We created a photoanode using the doctor-blade approach. For this purpose, a 25 nm transparent TiO_2 paste was applied as a dye absorbing layer on the FTO, followed by a 400 nm TiO_2 paste as a scattering layer to create an area of 0.16 cm^2 and an 8 µm thickness. After coating, the prepared photoanodes for annealing were heated to 500°C in a furnace with a balanced temperature gradient. After the photoanodes reached room temperature, they were treated using a 40 mM $TiCl_4$ aqueous solution at 70°C for 30 min. Next, it was heated to 500°C for 30 minutes before progressively recovering to RT. The surface of TiO_2 nanoparticles was encapsulated with N719 dye by exposing the photoanodes to 0.5 mM N719 ethanol in a dark environment and at RT for 18 to 24 h. Were prepared the counter electrode through by coating 10 mM H_2PtCl6 ethanol on a 0.6 mm diameter perforated FTO surface to cover the cathode surface completely. After layering, the cathode was heated for 15 min at 460°C before being gently brought to room temperature. The counter electrode

(cathode) and the working electrode (photoanode) were then joined using a 7-mm-thick Surlin polymer sheet. The sheet was heated to 120°C for 90 s and inserted between the two electrodes. Over the last stage, the electrolyte was completely infused into the area between the cathode and the photoanode. To this end, the electrolyte was poured over the hole in the cathode using a vacuum system. Similarly, four types of DSSCs were created by infusing four different electrolytes, of which one was a standard electrolyte and the other three were nanocomposite electrolytes.

2.6. Photovoltaic characterization

The constructed solar cells were irradiated in the presence of a solar light simulator (Sharif Solar, SIM-1000) with an intensity (1000 Wm^{-2}) equivalent to AM 1.5 solar spectrum irradiation. DSSCs' current-voltage (J-V) was measured using an IviumStat.XRe in the potential range of 0 to 150 mV, with a step size of 10 mV. The photovoltaic properties, including V_{OC}, J_{SC}, efficiency (η%), and fill factor (FF), were explored through the J-V curve analysis. The FF and η% were estimated based on the following formulas:

$$FF = \frac{P_{max}}{V_{OC} \times J_{SC}} = \frac{V_{max} \times J_{max}}{V_{OC} \times J_{SC}}$$

$$\eta(\%) = \frac{P_{max}}{P_{in}} \times 100\% = \frac{FF \times V_{OC} \times J_{SC}}{(100mW/cm^2)} \times 100\%$$

In the AC range of 20 mV and the frequency of 0.01-100 kHz, we measured the electrochemical impedance spectra (EIS) of DSSCs using a solar light simulator (Sharif Solar, SIM-1000) and IviumStat.XRe. The EIS experimental data were fitted with an equivalent circuit model in the ZView computer program. In this study, for each of the four electrolytes, three DSSCs were made. Finally, the electrochemical results for each type of DSSC with a given electrolyte were the average of the three DSSCs' results.

3. Results and discussion

In this study, an effective additive was prepared for DSSCs electrolyte by incorporating heterocyclic imidazole compounds and cobalt-transition metal complexes with pyridine heterocyclic ligands into graphene oxide's structure. The photovoltaic effectiveness of this chemical was explored as an effective additive in nanocomposite electrolytes in DSSCs after confirming the existence of particular components in the GO-VI/TBP cobalt complex structure.

3.1. Characterization of GO and GO-VI/TBP cobalt complex

FT-IR spectroscopy of GO and GO-VI/TBP cobalt complex is presented in Fig. 1. This graph can characterize the functional group and factors on graphene sheets. The typical O-H stretching band appeared at 3432 cm^{-1} in the GO spectra. In addition, a band at 1730 cm^{-1} related to carboxylic group C = O stretching and a band at 1625 cm^{-1} related to the C = C stretching have appeared. The C-O bond and the stretching of epoxy groups C–O–C are related to the bands generated in 1054 cm^{-1} and 1225 cm^{-1}, respectively [37, 38]. bands in the range of 571-733 cm^{-1} represent the fingerprint area in the GO-VI/TBP cobalt complex spectra. In addition, the bands at 657 cm^{-1} and 722 cm^{-1} are indexed to the production of cobalt complexes and organometallic linkages. The presence of nitrogen-rich GO-VI/TBP cobalt complex causes absorption bands in the band ranges of 830 cm^{-1} and 1498 cm^{-1}. The adsorption bands in 1227 cm^{-1} and 1417 cm^{-1} are indexed to C-N and C = N, respectively, suggesting the functionalization of GO-VI/TBP cobalt complex with pyridine and imidazole derivatives. The bands in the 1631 cm^{-1} and 1610 cm^{-1} range are because of the N-H, C-N, and C=C bonds, indicating a successful imidazole binding on GO-VI/TBP cobalt complex. After functionalization of the GO, the ensuing carboxylic group band in the GO spectra at 1728 cm^{-1} vanished. The highlighted binary bands around 2870 cm^{-1} and 2965 cm^{-1} correlate to

the stretching C-H in the GO-VI/TBP cobalt complex. The band corresponding to the O-H stretching in the GO-VI/TBP cobalt complex spectrum was superimposed with the N-H stretching bands. Next, it reappears at 3442 cm^{-1} after the functionalization of GO by adding imidazole and pyridine to the GO structure [22, 39-46]. In summary, the data obtained from the FT-IR indicate the proper completion of the GO functionalization.
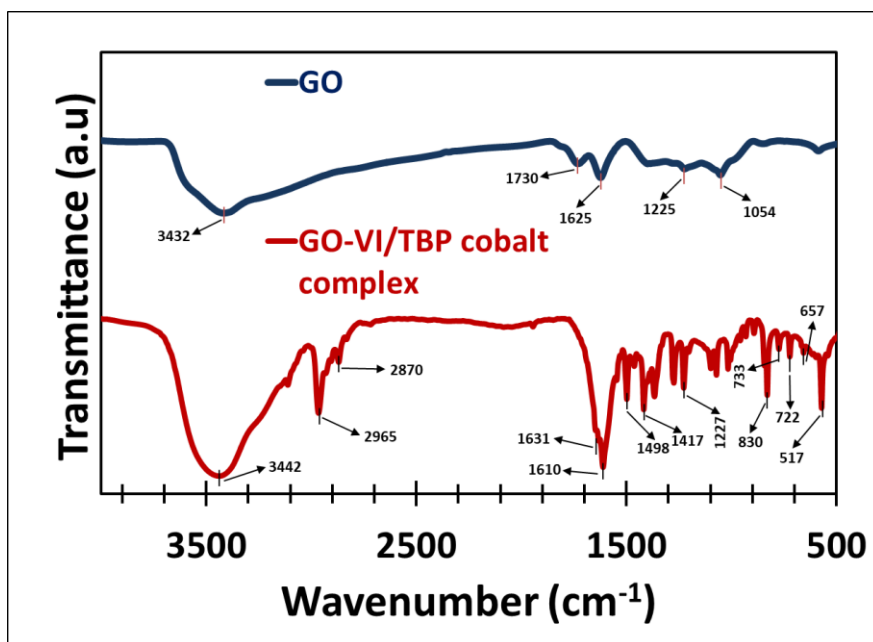
Fig. 1. The FT-IR of GO and GO-VI/TBP cobalt complex

Investigation and comparison of the exfoliation of GO and GO-VI/TBP cobalt complexes were done using X-ray powder diffraction. Fig. 2 depicts the XRD spectra of two GO and GO-VI/TBP cobalt complex instances in the 2θ range of 3° to 80°. The diffraction peak (001) in the XRD spectrum of GO occurred at 2θ =11° (indicating a 0.76-nm interlayer distance) and the peak at 2θ =43° (indicating a 0.21-nm interlayer distance). This interlayer gap is due to the oxygenated functional groups observed on the GO surface layers, such as hydroxyl, carbonyl, and epoxide. The GO peaks indicate a scattering following the functionalization with cobalt complexes. According to the XRD spectrum of the GO-VI/TBP cobalt complex, the peak diffraction appeared

at 2θ =16.92°. The GO interlayer distance was also reduced to 0.52 nm, suggesting the successful reduction process in GO [22, 47-50]. Additionally, 2θ = 17° and 2θ = 18° peaks can be linked to different functional groups that establish chemical interactions between GO and cobalt complexes, as well as ligands in cobalt complexes, to form GO-VI/TBP cobalt complex.
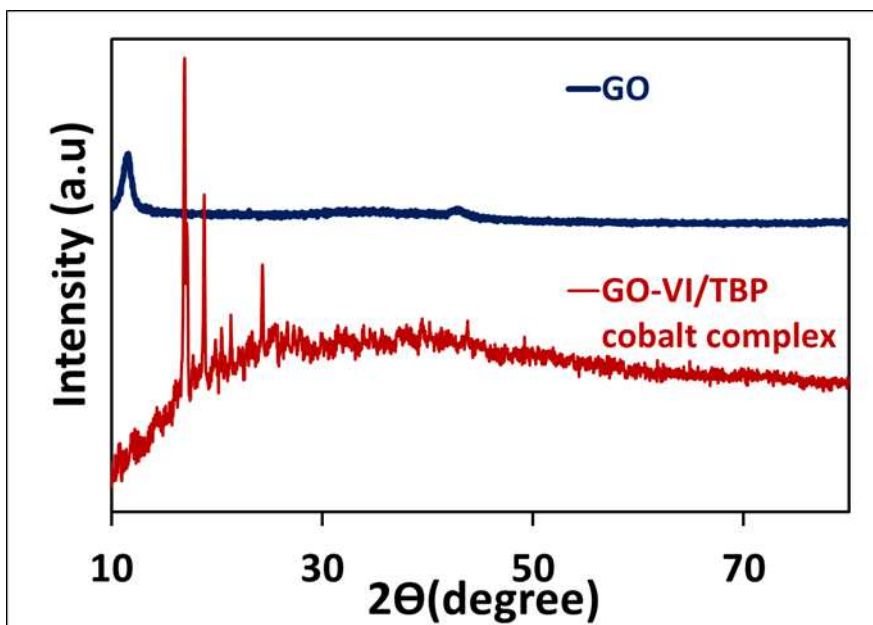
Fig. 2. XRD patterns of GO and GO-VI/TBP cobalt complex
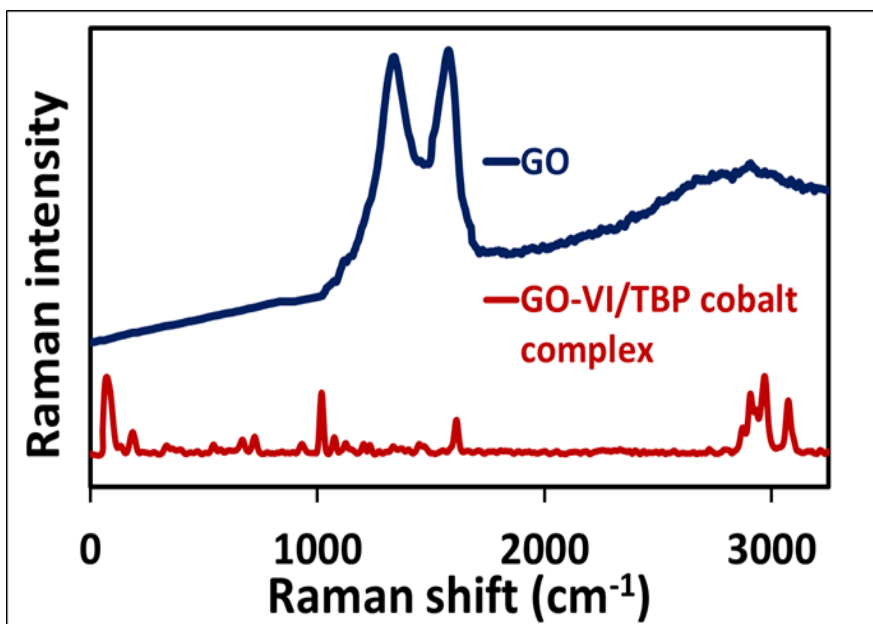
Fig. 3. Raman spectra corresponding to GO-VI/TBP cobalt and GO complex

The Raman spectra of GO and GO-VI/TBP cobalt complex are shown in Fig. 3. The two primary properties of GO may be detected in the GO spectra at 1583 cm^{-1} (G band) and 1346 cm^{-1} (D band). Carbon atoms' stretching vibration in sp^3 is represented by the D band. This band corresponds to the state of kpoint phonons in A_{1g} symmetry. Also, carbon atoms' stretching vibration in the sp^2 is visible in the G-band, which is associated with the E_{2g} state. The graphene monolayers, considered impurities in the GO structure, are also linked to the two relatively faint peaks of roughly 2700 cm^{-1} and 2900 cm^{-1}. The Raman spectrum of GO-VI/TBP cobalt complex changes with functionalization and insertion of different functional groups into the GO structure. The symmetric stretching vibrations of CH_3 and CH_2 were linked to the peaks in 2800-3000 cm^{-1}. In addition, the stretching C=C corresponds to the peak appearing in the 1600 cm^{-1} region. The peak at 1018 cm^{-1} is indexed to C-N symmetric stretching bond in heterocyclic rings. The peak at 930 cm^{-1} is also related to the C-C symmetric stretching bond. Finally, the peaks in 500 cm^{-1} to 1000 cm^{-1} range are because of cobalt complexes bonds [41, 51-54].

XPS is an efficient tool for studying material chemical composition [26]. In this study, the chemical structure of the synthesized complex was investigated using the XPS analysis for the GO-VI/TBP cobalt complex. Fig. 4(a) shows the obtained XPS survey spectra. Categorizing the obtained peaks indicate the presence of chlorine, carbon, nitrogen, oxygen, and cobalt atoms, confirming the successful synthesis of the GO-VI/TBP cobalt complex. Based on their area peaks in the XPS spectrum, the atomic percentages of samples were estimated. The results are given in Table 1.

Table 1. The atomic percentage of prepared samples based on the XPS spectra

Sample name	Area (atomic percentage)				
	Cl	C	N	O	Co
GO-VI/TBP cobalt complex	5.28	43.74	16.64	17.41	16.94

Fig. 4(b) presents the high-resolution XPS spectrum of Co 2p. In this figure, the peaks of Co $2p_{3/2}$ and Co $2p_{1/2}$ appear at 780.9 and 796.6 eV, respectively. The energy difference (spin-orbit splitting) between those peaks was 15.7 eV, which is close to the standard value. Therefore, this observation confirms that cobalt complexes have formed on the surface of functionalized GO [22, 55, 56]. The Cl 2p spectrum (Fig. 4(c)) is fitted with two sharp peaks at 199.3 and 197.7 eV binding energies, corresponding to Cl $2p_{3/2}$ and Cl $2p_{1/2}$. In the XPS spectrum of C 1s (Fig. 4(d)), the peaks appeared at 284.3 eV, 285.8 eV, and 288.9 eV can be ascribed to C-C/C=C, C-O/C-N, and π-π interaction of functionalized GO, respectively [57-61]. In Fig. 4(e), the XPS spectrum of O1 s turned into three components: O-C/O=C bonds at 531.1 eV, carboxylate oxygen at 532.1 eV, and Co-O bonds at 533.0 eV. Also, the high-resolution XPS spectrum of N1s (Fig. 4(f)) was deconvoluted into two peaks, i.e., the C-N bonds of the imidazole moiety (398.9 eV) and the Co-N bonds of the cobalt complex on the surface of modified GO (405.4 eV).
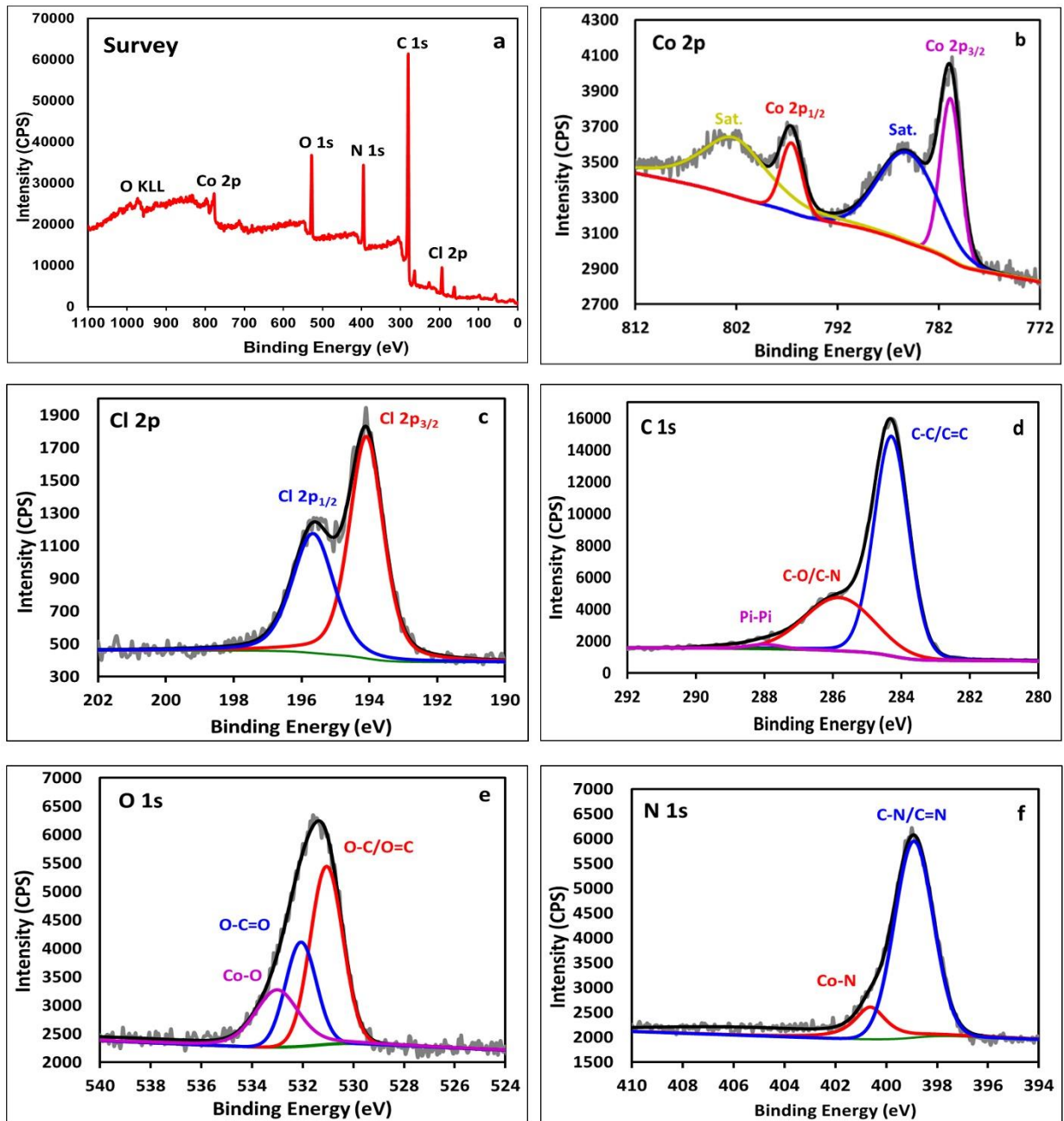
Fig. 4. XPS spectra corresponding to (a) survey, (b) Co 2p, (c) Cl 2p, (d) C 1s , (e) O 1s, and (f) N 1s of GO-VI/TBP cobalt complex

Fig. 5(a) and (b) present field emission scanning electron microscopy (FESEM) images of GO-VI.

Also, Fig. 5(c) and (d) show FESEM images of GO-VI/TBP cobalt complex. The morphology of

GO sheets functionalized with the chemical compound 1-vinylimidazole is depicted in Fig. 5(a) and (b). At this point, the GO structure has wrinkles that can generate a channel that speeds up ion diffusion. Fig. 5(c) and (d) depict how the morphology of GO sheets has changed since they were functionalized with cobalt complexes, as opposed to the images in Figures 5(a) and (b). Fig. 5(c) and (d) shows the modification of GO sheets after its functionalization with cobalt complexes, that morphology has changed compared to the images in Fig. 5(a) and (b). The state of edge wrinkles changes after cobalt complexes are used to modify GO surfaces and the GO-VI/TBP cobalt complex, that has better ion transport capabilities than GO-VI, is synthesized. The composition of the elements in the structure of the GO-VI/TBP cobalt complex was determined through the energy-dispersive X-ray (EDX) mapping analysis, as shown in Fig. 7. The EDX-mapping image demonstrates that cobalt complexes with various ligands have been effectively inserted into the GO structure. This figure shows carbon, chlorine, cobalt, nitrogen, and oxygen in the GO-VI/TBP cobalt complex structure as weight percentages with distinct hues [22].
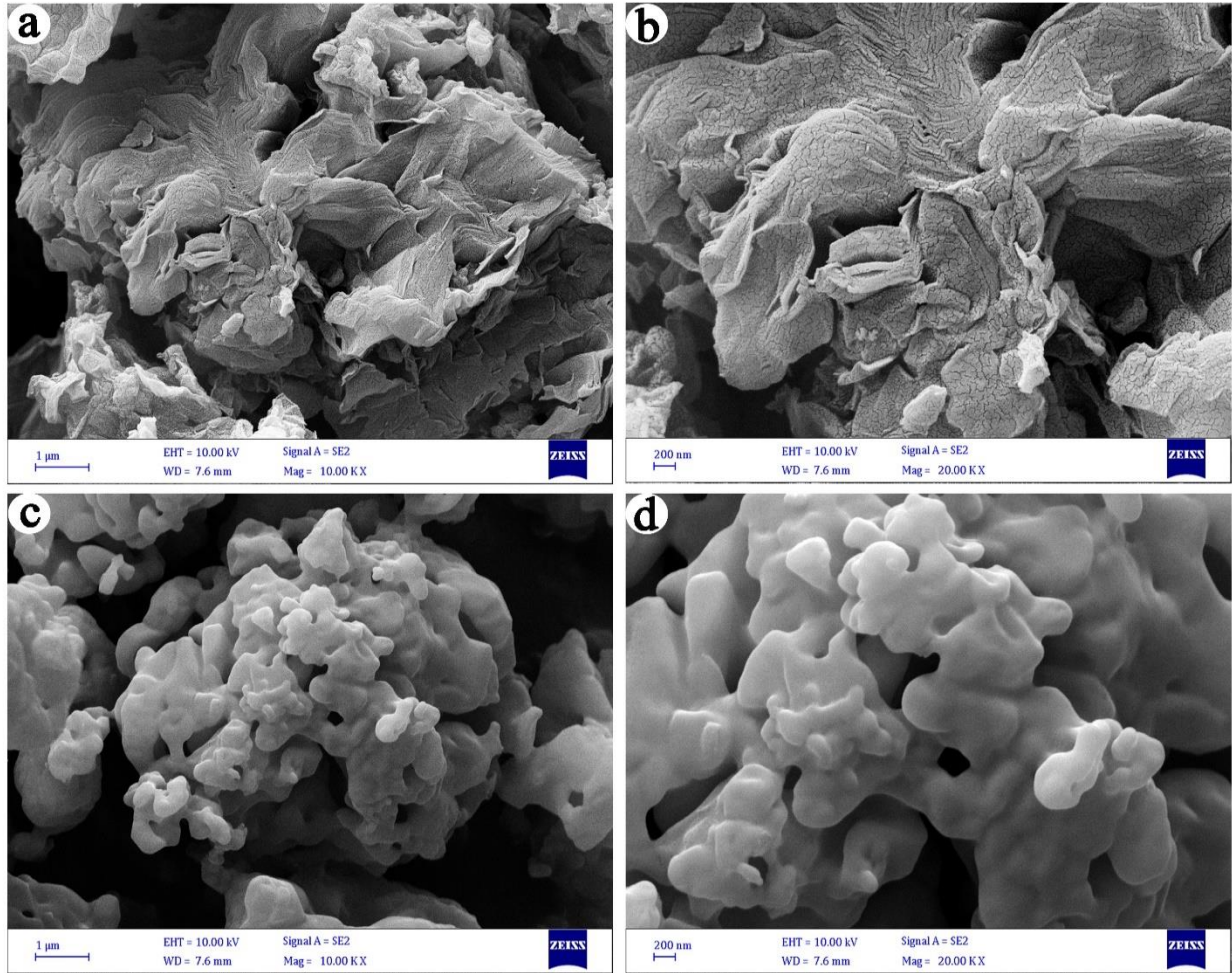
Fig. 5. (a) and (b) FESEM images of GO-VI, (c) and (d) FESEM images of GO-VI/TBP cobalt complex

The thin and transparent morphology of the GO-VI/TBP cobalt complex nanosheets can be seen in the transmission electron microscopy (TEM) images presented in Fig. 6. The functional groups that entered the GO structure after functionalization are also represented by the dark textured portions. [22, 62-64].
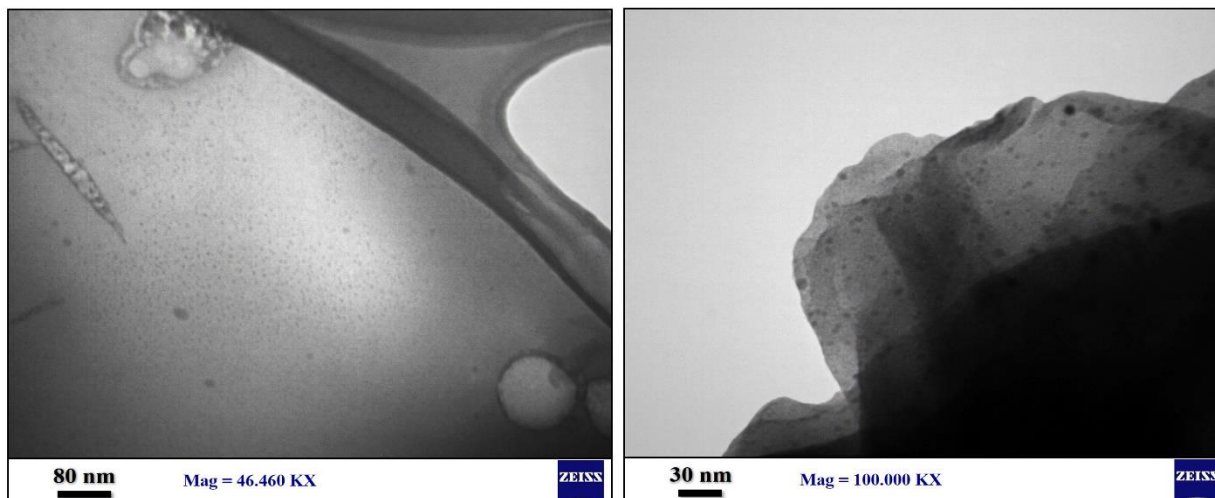
Fig. 6. TEM images of GO-VI/TBP cobalt complex
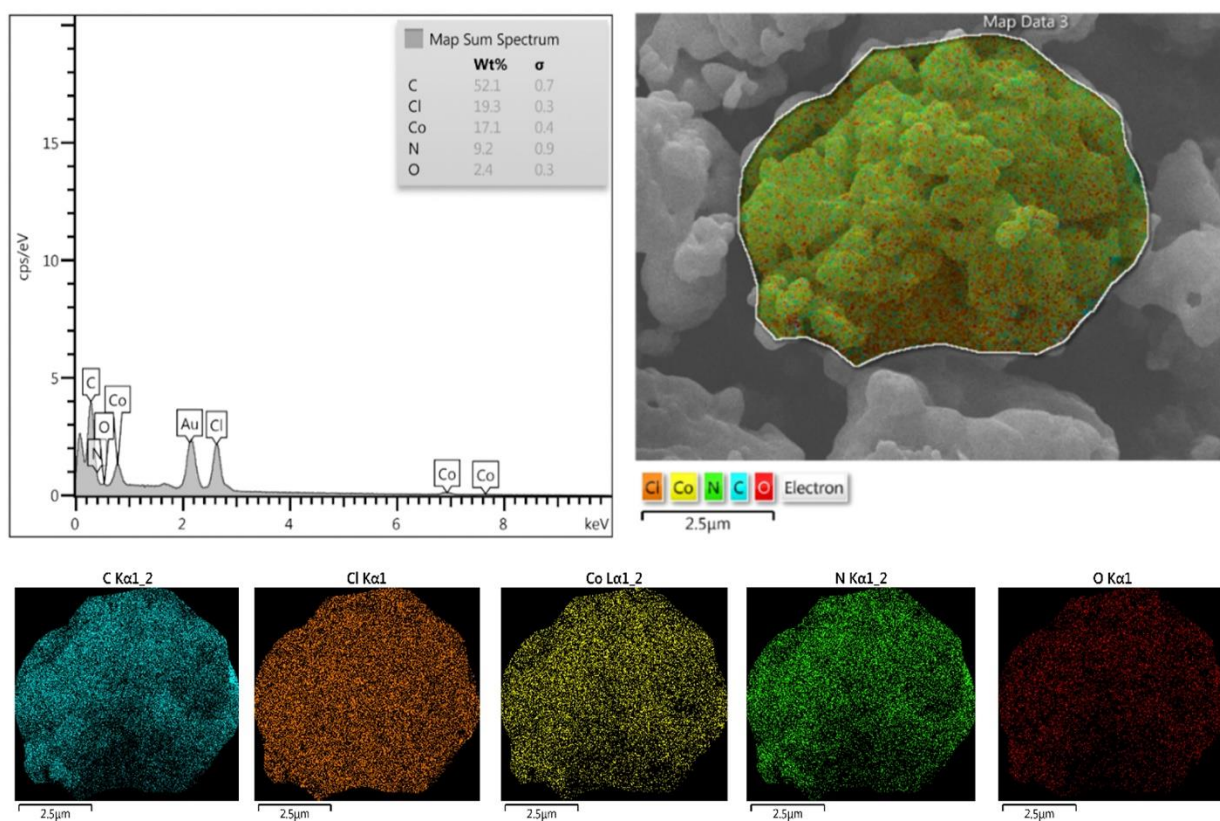
Fig. 7. EDX mapping analysis of GO-VI/TBP cobalt complex

3.2. DSSCs' photovoltaic performances with new electrolytes

The efficiency of DSSCs in terms of photovoltaics was investigated by preparing different electrolytes based on BMII and EMII ILs with various percentages of effective additives of GO-VI/TBP cobalt complex. The results are presented in the form of the J-V curve in Fig. 8(a) based on the photovoltaic values in Table 2. The least efficient DSSCs are those constructed of E0 electrolyte with 0% effective additive (standard electrolyte). Compared to DSSCs with nanocomposite electrolytes, DSSCs with standard electrolyte have the lowest J_{SC} (8.131 mA cm^{-2}), lowest V_{OC} (0.725 V), and lowest efficiency (η = 4.130%), demonstrating that DSSCs with E0 electrolyte has no amplifier. The efficiency of DSSCs was significantly increased from η=4.130% to η=6.640% by adding 0.3 wt.% GO-VI/TBP cobalt complex to the electrolyte (E2), changing the J_{SC} from 8.131 mA cm^{-2} to 12.975 mA cm^{-2}, the V_{OC} from 0.725 V to 0.751 V. The cobalt complexes and nitrogen heterocyclic compounds in the GO-VI/TBP cobalt complex decrease the ohmic contact resistance when the amount of GO-VI/TBP cobalt complex in the electrolyte increases by 0.3 wt.%. The values of V_{OC} and J_{SC} rise due to this resistance drop because it increases electron transport and accelerates the redox process. The FF drop following the addition of the GO-VI/TBP cobalt complex to the electrolyte is attributed to the rise in the electrolyte viscosity and the increase in the interaction between FGO and the imidazolium ILs-based electrolyte. DSSCs with electrolytes containing 0.6 wt.% (E3) and 0.9 wt.% (E4) GO-VI/TBP cobalt complex as an effective additive were also investigated. The highest quantity of GO-VI/TBP, and therefore the best efficiency, is observed in the electrolyte medium in DSSCs with E3 electrolyte. This complex interacts with ionic liquids, forming the most significant electron and ionic conductivity in the electrolyte medium. Since DSSCs with the E3 electrolyte had the highest efficiency among all DSSCs, their efficiency increased by 78.18% (i.e., from 4.130% to 7.359%)

compared to the standard electrolyte (E0). The J_{SC} value increased from 8.131 mA cm^{-2} to 14.301 mA cm^{-2}, and the V_{OC} value increased from 0.725 V to 0.754 V. In addition, the DSSCs with the E4 electrolyte had a photovoltaic efficiency of 6.162%, a V_{OC} of 0.735 V, and a J_{SC} of 12.340 mA cm^{-2}. The efficiency reduction and, consequently, the decrease in J_{SC} and V_{OC} values when using 0.9 wt.% compared to 0.6 wt.% is due to the difficulty of ion transfers rising with the quantity of GO-VI/TBP cobalt complex in the electrolyte and the significant rise in the viscosity of the electrolyte medium. In general, there is a considerable improvement in the performance of DSSCs when using nanocomposite electrolytes with GO-VI/TBP cobalt complex as an effective additive compared to the standard electrolyte without GO-VI/TBP cobalt complex. This improvement is attributed to the GO-VI/TBP cobalt complex's features by enhancing the charge transfer in the electrolyte and producing cohesion.
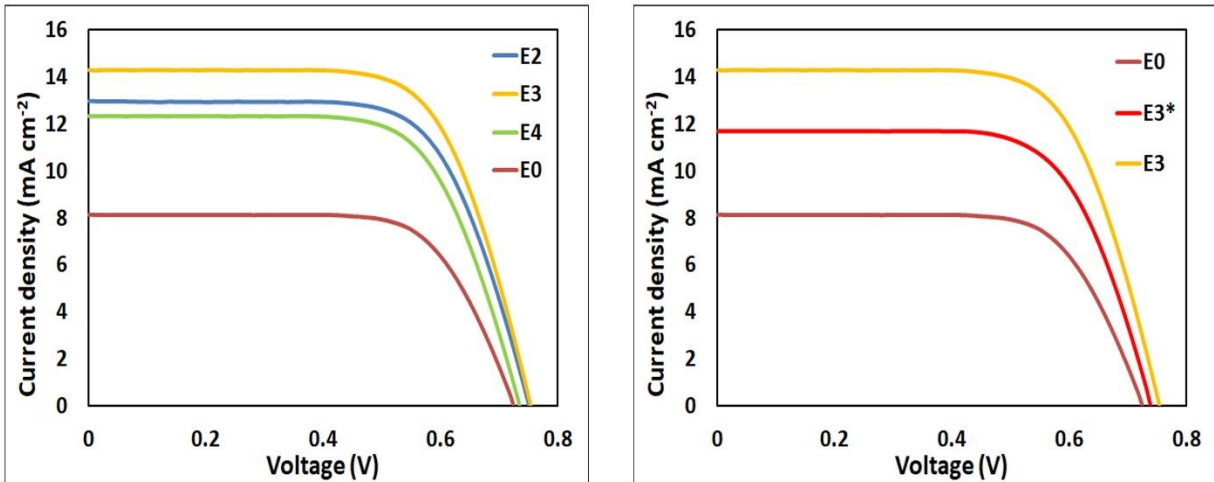
Fig. 8. Curves of current density-voltage (J-V) characteristics for (a) DSSCs based on different amounts of GO-VI/TBP cobalt complex in electrolytes (i.e., E2, E3, and E4), and the standard electrolyte (E0); (b) DSSCs based on electrolyte (E3), electrolyte (E3*), and standard electrolyte (E0)

Table 2. Photovoltaic parameters obtained from J-V curves of DSSCs based on different amounts of GO-VI/TBP cobalt complex in electrolytes (i.e., E2, E3, and E4), and the standard electrolyte (E0)

Cell	η [%]	FF	J_{SC}[mA/cm^2]	V_{OC}[V]
E0 (0 wt.% GO-VI/TBP cobalt complex)	4.130	0.701	8.131	0.725

E2 (0.3 wt.% GO-VI/TBP cobalt complex)	6.640	0.681	12.975	0.751
E3 (0.6 wt.% GO-VI/TBP cobalt complex)	7.359	0.682	14.301	0.754
E4 (0.9 wt.% GO-VI/TBP cobalt complex)	6.162	0.679	12.340	0.735

The present study addresses the effect of cobalt complexes in the structure of GO-VI/TBP cobalt complex on the performance of DSSCs compared to GO-VI. In GO-VI, GO has just been functionalized with 1-vinyl imidazole and has not yet reacted with TBP and $CoCl_2$. The photovoltaic outcomes of the two types of electrolytes used in DSSCs were compared with the same quantity of effective additive (0.6 wt.%). The comparative value of 0.6% was chosen as it yielded the largest return in the previous phase. The first and second electrolytes were different such that GO-VI/TBP cobalt complex was used as an effective additive in one, while GO-VI was used in the other. DSSCs with standard electrolyte (E0) have the lowest efficiency compared to the two types of DSSCs that contain GO-VI/TBP cobalt complex and GO-VI as an effective additive (Fig. 8(b) and Table 3). According to the results, DSSCs with E3 electrolyte that use GO-VI/TBP cobalt complex as an effective additive outperform DSSCs with electrolyte (E3*) that use GO-VI. In DSSCs with E3 electrolyte, a η of 7.359, J_{SC} of 14.301 mA cm^{-2}, and V_{OC} of 0.754 V were obtained. Also, in DSSCs with E3*electrolyte, a photovoltaic efficiency of 5.896, J_{SC} of 11.703 mA cm^{-2}, and V_{OC} of 0.739V were obtained. In contrast to DSSCs with E0 electrolyte, the amount of J_{SC} and V_{OC} and the efficiency of the process increase in DSSCs with E3* electrolyte due to increased electron transfers caused by the presence of GO and nitrogen-containing heterocyclic compounds. The efficiency of DSSCs with E3 electrolyte was higher than DSSCs with E3* electrolyte due to the cobalt complexes added to the GO-VI structure. When cobalt complexes with TBP ligand are present in the electrolyte E3, V_{OC} and J_{SC} rise along with the redox

reaction rate, thereby increasing the efficiency of DSSCs with E3 electrolyte compared to DSSCs with E3* electrolyte.

Table 3. Photovoltaic parameters obtained from J-V curves of DSSCs based on electrolyte (E3), electrolyte (E3*), and standard electrolyte (E0)

Cell	η [%]	FF	J_{SC} (mA/cm^2)	V_{OC} [V]
E0 (0 wt.% GO-VI/TBP cobalt complex/ GO-VI)	4.130	0.701	8.131	0.725
E3 (0.6 wt.% GO-VI/TBP cobalt complex)	7.359	0.682	14.301	0.754
E3* (0.6 wt.% GO-VI)	5.896	0.682	11.703	0.739
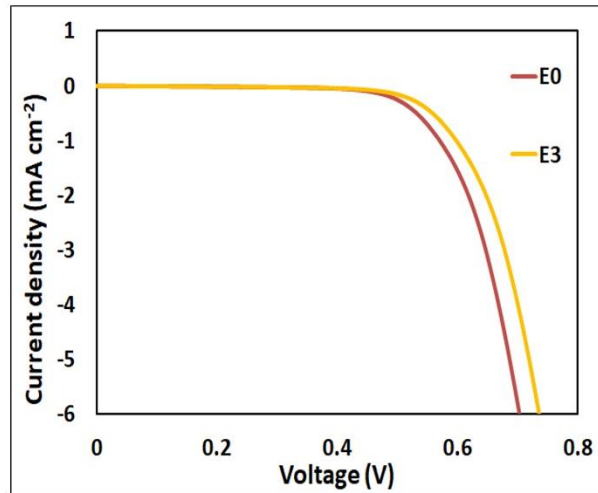
Fig. 9. The dark J-V curves of DSSCs based on electrolyte (E3) and standard electrolyte (E0)

The recombination process in DSSCs was studied using dark J-V curves. DSSCs function as a diode in the dark. Fig. 9 depicts dark current J-V curves of two types of DSSCs, one with standard electrolyte (E0) and the other with 0.6 wt.% GO-VI/TBP cobalt complex electrolyte (E3). According to the dark DSSCs J-V curves, the amount of V_{OC} in DSSCs with E3 electrolyte is larger than in DSSCs with E0 electrolyte. The low recombination electrons in these DSSCs account for the high V_{OC} value in dark current density-voltage curves. According to these observations, the

presence of GO-VI/TBP cobalt complex in the electrolyte as an effective additive lowers the recombination degradation process in DSSCs. Given that TBP can decrease the destructive process of recombination and increase V_{OC} in DSSCs, its inclusion in GO-VI/TBP cobalt complex as a ligand of cobalt complexes makes GO-VI/TBP cobalt complex an effective additive in DSSCs with E3 electrolyte to minimize the destructive process of recombination more effectively.

3.3. Electrochemical performances of DSSCs

The electron transitions and the impacts of these transfers by the electrolyte in DSSCs were investigated using an electrochemical impedance spectroscopy approach. Two types of DSSCs were evaluated for this objective: one with a standard electrolyte (E0) and the other with a 0.6 wt.% GO-VI/TBP cobalt complex electrolyte (E3). Fig .10 illustrates the Nyquist plots of two DSSCs with different electrolytes. The figure also represents the equivalent circuit model applied to fit the experimental EIS data with ZView software. Two semicircles and a Warberg line appeared after fitting the experimental data, as shown in Fig. 10. In this case, R_1 is the resistance corresponding to the counter electrode, R_2 is the resistance corresponding to dye/TiO$_2$/electrolyte, R_{Diff} is Warberg resistance related to the process of redox pair (I$^-$/I$_3^-$) diffusion in the electrolyte, and R_S denotes series resistance, including joints and TCO layers' resistance. In the Nyquist plots of DSSCs, semicircles with a wider radius were produced with E0 electrolyte compared to the DSSCs with E0 electrolyte. Regarding the semicircles of DSSCs with E0 electrolyte's huge radius, Table 4 shows that in DSSCs with a standard electrolyte (E0), R_S, R_1, R_2, and R_{Diff} are higher than in DSSCs with a 0.6 wt.% GO-VI/TBP cobalt complex electrolyte (E3). The GO-VI/TBP cobalt complex effective additive in the nanocomposite electrolyte, which makes the largest contribution to the charge transfer process, may cause variations in R_1 and R_2. By enhancing the electrocatalytic activities between the electrolyte and Pt, the presence of GO-VI/TBP cobalt complex in the

structure of the E0 electrolyte decreased the R_1 in addition to increasing J_{SC}. Considering the improved charge transfer channels and the efficient interaction of the electrolyte with TiO_2, the charge transfer resistance associated with TiO_2 and the electrolyte (i.e., R_2) also decreased in the presence of the GO-VI/TBP cobalt complex. Regarding the unique properties of GO, heterocyclic nitrogen compounds, and cobalt complexes, the addition of GO-VI/TBP cobalt complex as an effective additive in the E3 electrolyte increases the diffusion process and conductivity in the electrolyte. As a result, the R_{Diff} value decreases compared to the E0 electrolyte. Generally, the presence of GO-VI/TBP cobalt complex as an effective additive in the electrolyte composition reduces overall DSSCs resistance while increasing efficiency and performance. It is of note that using ILs-based electrolytes in all DSSCs has made them more stable by lowering electrolyte leakage. Furthermore, the DSSCs, which were the topic of the study, are among the most environmentally friendly and green solar cells because of their compatibility with the environment and sustainability with this type of electrolyte.
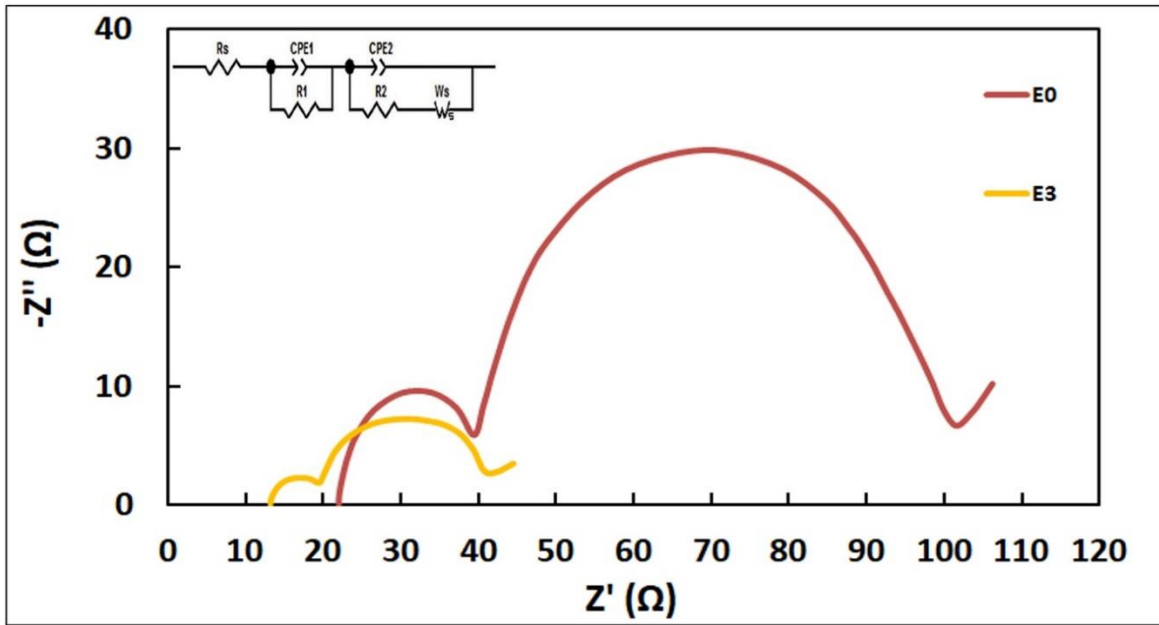
Fig. 10. EIS spectrum of DSSCs based on a new nanocomposite electrolyte (E3) and a standard electrolyte (E0)

Table 4. EIS parameters obtained by fitting the experimental data using ZView software

Cell	R_S (Ω)	R_1 (Ω)	R_2 (Ω)	R_{Diff} (Ω)
E0 (0 wt.% GO-VI/TBP cobalt complex) **(Standard electrolyte)**	22.03	17.21	65.76	74.52
E3 (0.6 wt.% GO-VI/TBP cobalt complex) **(New nanocomposite electrolyte)**	13.21	6.29	21.82	27.46

3.4. Computational calculations

3.4.1. DFT Method

Calculations corresponding to Density functional theory (DFT) [65, 66] were used to show how incorporating GO-VI/TBP cobalt complex as an efficient additive to electrolytes enhances DSSCs' efficiency. The Vienna ab initio simulation package (VASP) [67, 68] was applied using the plane-wave basis set and the generalized gradient approximation (GGA) [69] by the Perdew-Burke-Ernzerhof (PBE) [70]. The projected-augmented wave (PAW) [71] method was used for dispersion correction [72]. The electronic wave function in the plane wave basis sets was expanded using cutoff energy of 500 eV. Also, the irreducible Brillouin zone was sampled by the Γ point grid of the Monkhorst Pack scheme [73] for the slab model of the structures.

3.4.2. DFT Model

According to the literature [74-76], anatase TiO2 (101) facets are more thermodynamically stable. Hence, they were also chosen in our investigation. The geometries of the adsorbed structures of ILs and TBPs molecules on TiO_2 (101) surface were optimized, Fig. 11(a). To better understand the electronic structures of the interfaces of TiO_2 (101) electrode and the electrolyte additive used in this study, we also created and optimized the adsorbed structures of GO-VI in the presence of

TBPs on the surface of TiO_2 (Fig. 11(b)). The adsorption of GO-VI/TBP cobalt complex on TiO_2 (101) was also investigated and shown in Fig. 11(c).

We obtained equilibrium lattice constants of a,b = 3.784 Å and c = 9.514 Å for bulk TiO_2 anatase, which agree well with the results of an experimental study [77]. The anatase TiO_2 (101) surfaces were modeled by a slab including 288 atoms with a 2×3 periodicity (Fig. 11). A vacuum space larger than 10 Å between TiO_2-additive assembly is introduced to avoid interaction between periodic images. Slab thickness of eight atomic layers in the z-direction was used to model the anatase surfaces in line with previous calculations [78, 79]. In this design, four bottom layers are frozen in the bulk geometry, while the others are relax-free. This resting is continued until each atom's maximum force and energy converge to 0.01 eV/Å and 10^{-5} eV, respectively.

We first investigated the interaction of the TiO_2 surface with ILs/TBPs molecules (Fig. 11(a)). To model the GO-VI in the presence of TBPs, we first created a GO layer with two sides decorated with hydroxyl and carboxyl functional groups randomly at the edges. Next, VI and TBP molecules were added to the GO layer, and their interactions with the TiO_2 surface were investigated (Fig. 11(b)).

The behavior of interface of GO-VI/TBP cobalt complex with TiO_2 surface was also investigated (Fig. 11(c)) using the same number of ILs and TBPs molecules in all studied electrolytes.
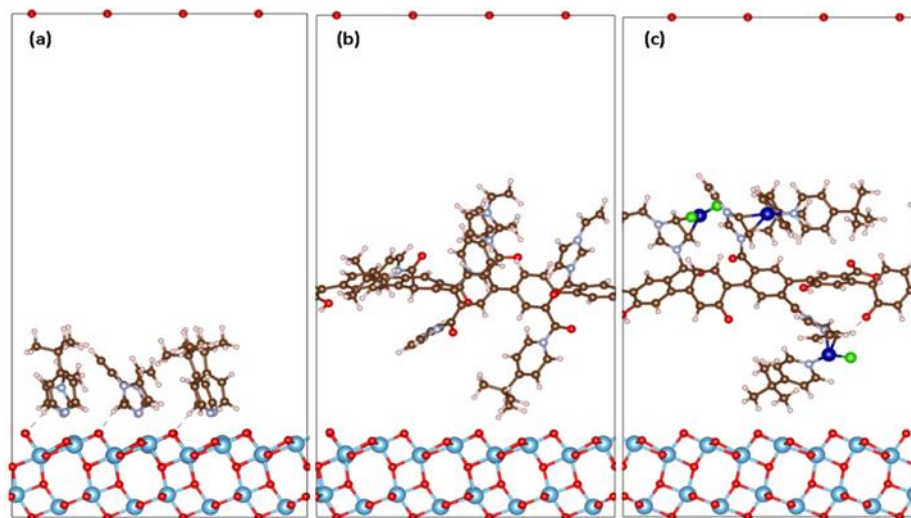
Fig. 11. The lowest energy adsorption structures of a) ILs/TBPs, b) GO-VI with TBP, and c) GO-VI/TBP cobalt complex on anatase TiO_2 (101) surface; carbon atoms are denoted in brown, oxygen in red, titanium in large blue, nitrogen in small blue, cobalt in dark blue, chlorine in green, and hydrogen in white spheres

3.4.3. DFT Results

In this research, VASP was applied to address the effect of additives, including GO layers filled by VIs and TBPs, in the presence and absence of cobalt complexes on the TiO_2 surface. We also studied electronic properties for the surface of clean anatase TiO_2 (101) and the adsorption configurations of the ILs/TBPs, GO-VI with TBPs, and GO-VI/TBP cobalt complex to explore the interactions between the electrolyte and its components and the surface of the electrode (TiO_2). Fig. 12 shows the projected density of states (PDOS) for the TiO_2 surface and the electrolyte additives. The results show an upward shift for the TiO_2 surface's conduction band after electrolyte additive adsorption on the surface. The conduction band for clean surface appeared at 2.0 eV, where it increased to 2.22, 2.28, and 2.35 eV after adsorption of the ILs/TBPs, GO-VI with TBPs, and GO-VI/TBP cobalt complex, respectively. As a result, electrons quickly penetrate from the dye LUMO to TIO_2's conduction band (101) [80].

Also, there are midgap states in the TiO_2 band gap above the valence band maximum (VBM) due to GO-VI with TBPs and GO-VI/TBP cobalt complex adsorption, thereby reducing the TiO_2 bandgap. The reduction of the total calculated bandgap through additive adsorption can lead to a redshift in the adsorption edge and enhance the efficiency of DSSCs.
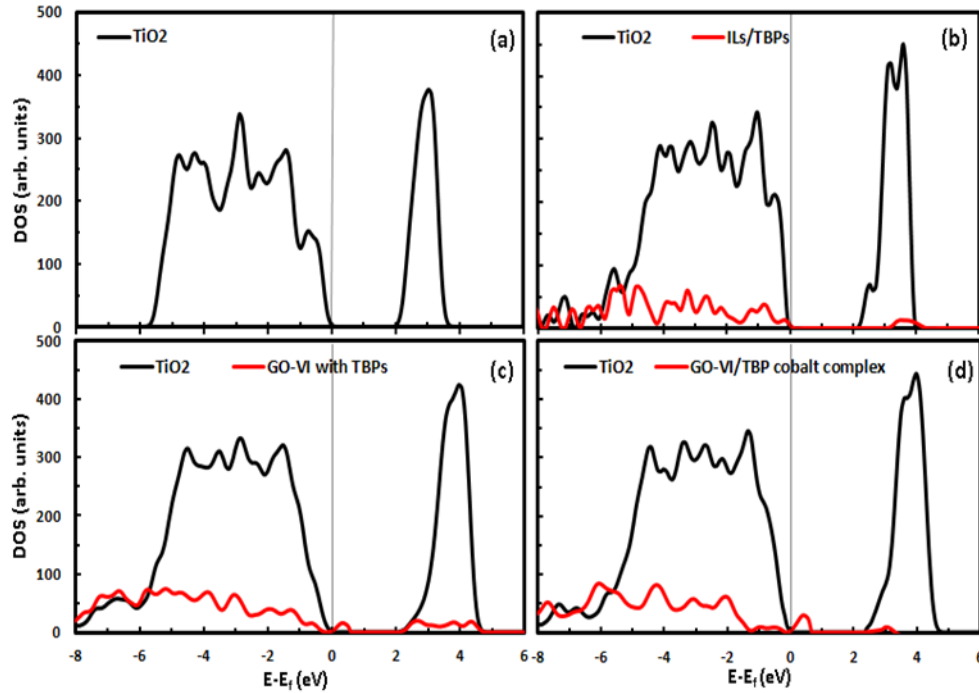
Fig. 12. The calculated PDOS for anatase TiO_2 (101) surface and the electrolytes in a) clean anatase TiO_2 (101) surface, b) TiO_2/ILs/TBPs, c) TiO_2/GO-VI with TBPs, and d) TiO_2/GO-VI/TBP cobalt complex (Fermi level is at 0 eV)

3.4.4. Artificial Intelligence method

The k-fold method was used to train and test the research data, and the k value is set to 10 based on a trial and error approach. All machine learning practices were done in the WEKA 3.9 software. The random seed value for XVal/% split is set to 1 during the calculation process for all algorithms, including RT, RF, SMOreg, GP, MP, and MB.

3.4.5. Artificial Intelligence results

In this section, data analysis was performed for the exact determination of data distribution (Fig. 13). As can be seen, predicting experimental features (V_{OC} and J_{SC}) based on simple curve-fitting regression models or classical computations is complex and almost impossible.
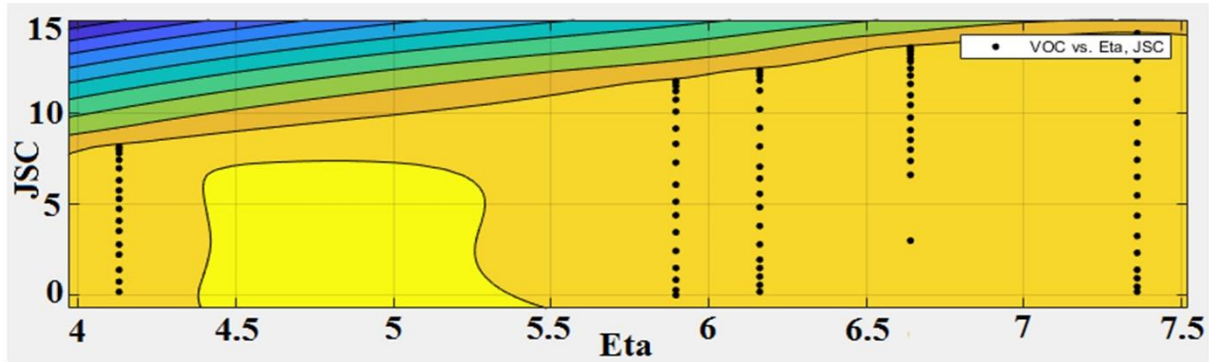
(a)
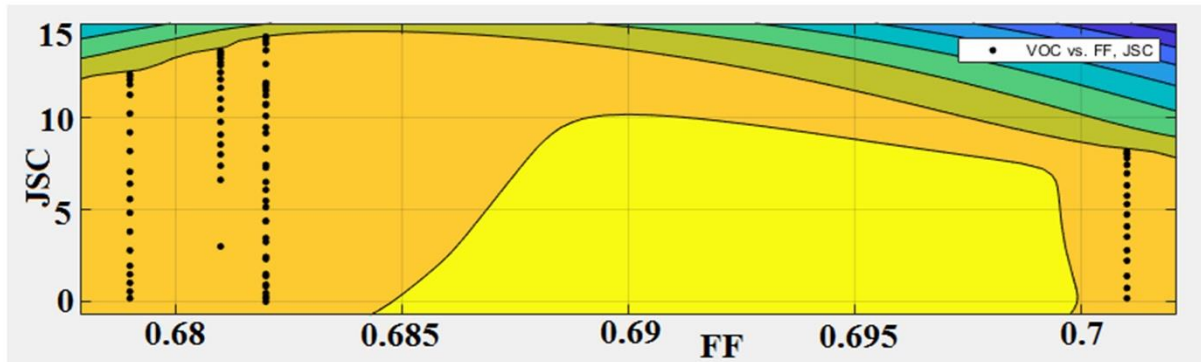
(b)
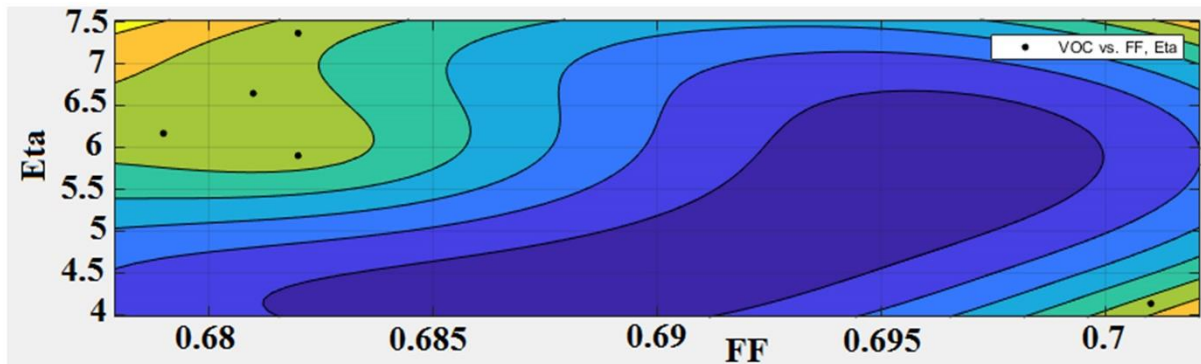
(c)

Fig.13. Data distribution analysis between computational and experimental features in the present research as per (a) V_{OC} vs Eta-J_{SC}, (b) V_{OC} vs FF-J_{SC}, and (c) V_{OC} vs Eta-FF

By applying machine learning computations, a soft sensor is designed to measure experimental features, including J_{SC} and V_{OC}, as per theoretical parameters. Therefore, a low-cost, highly efficient, and soft computing-based system was developed in the present field. Based on this concept, the smart operation of nanomaterial-based energy systems can be executed with a minimum investment cost [81-84]. The structure of the declared soft-sensor is illustrated according to Fig. 14. In this scheme, additive type, additive percentage, FF, and Eta are constant model inputs. Meanwhile, when the V_{OC} is presented, the J_{SC} is considered the input, and vice versa.
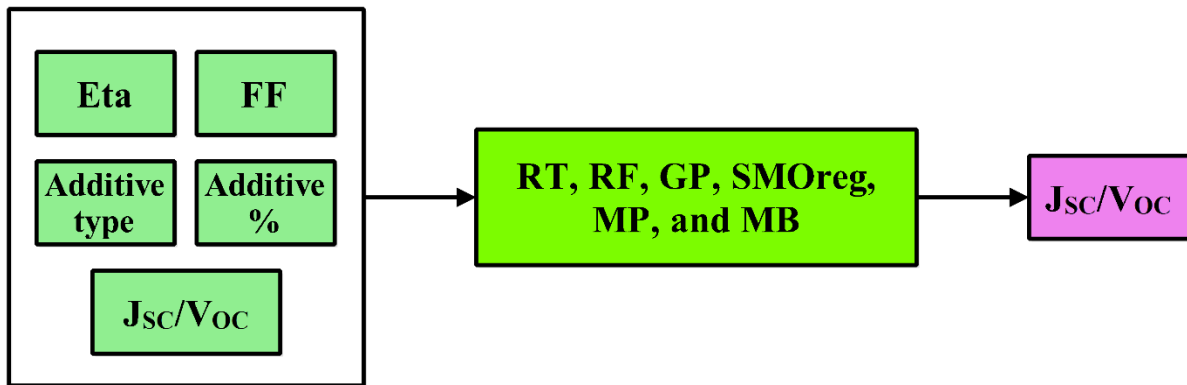
Fig. 14. Structure of machine learning computations in the present research

In the following, before conveying the machine learning computations' outputs, the heat maps of data distributions are illustrated in Fig. 15. The specifications of the databank are demonstrated in this scheme. Tables 2 and 3 show additive percentages range and their types, including GO-VI/TBP cobalt complex (type 1) and GO-VI (type 2).
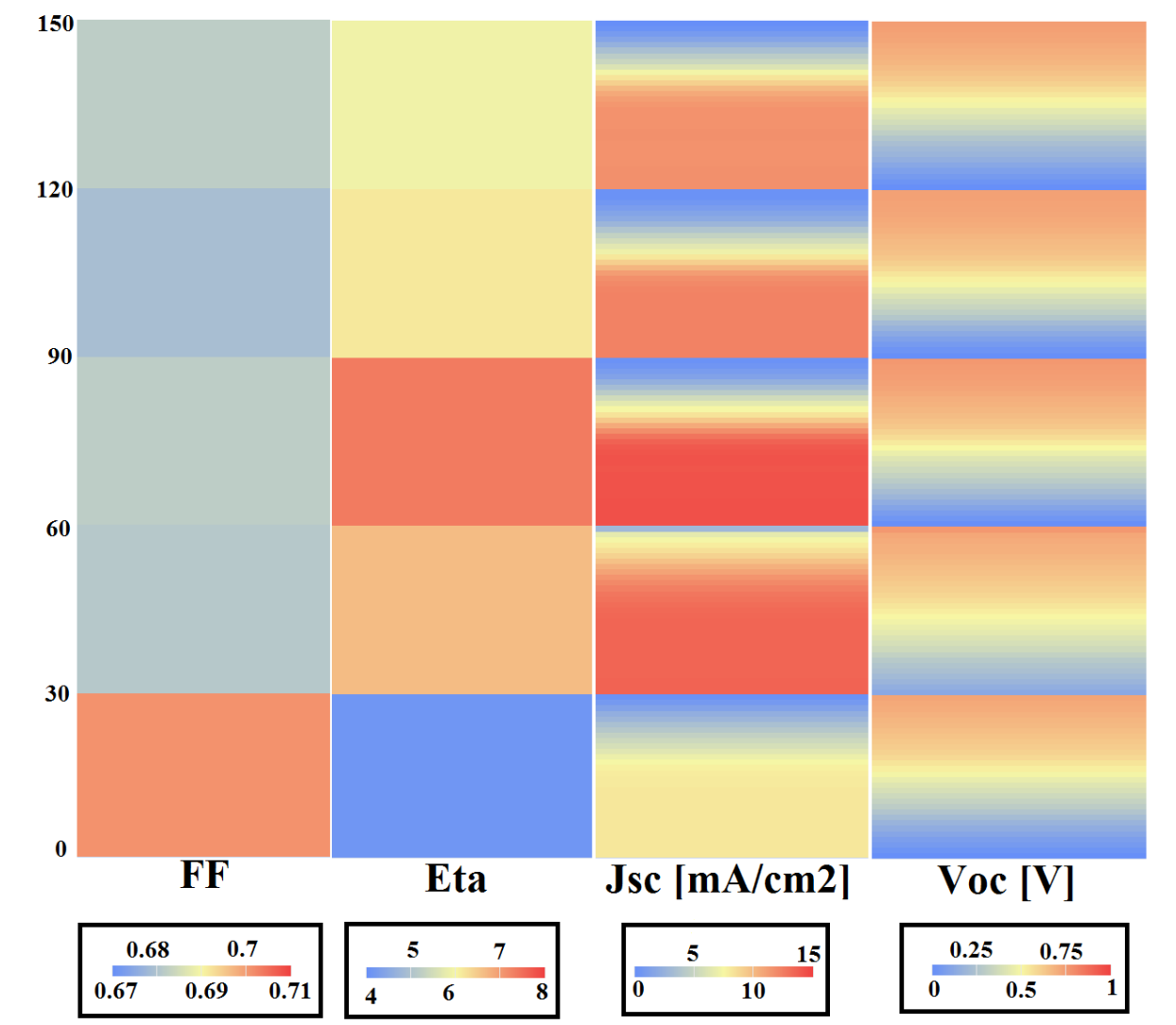
Fig. 15. The applied raw data in the machine learning process of the present study

In the first step of machine learning modeling and computations, V_{OC} is assumed as outputs, and other features are as inputs. With this hypothesis, the modeling outcomes are illustrated in Table 5. Based on the obtained results, it can be understood that RT and RF algorithms with a 0.93 correlation coefficient have the most precision for predicting V_{OC} based on effective features. On the other hand, the minimum efficiency is related to the GP algorithm with a 0.7 regression coefficient.

Table 5. Statistical indicators of different prediction algorithms based on V_{OC} as output

Statistical parameters	RT	RF	GP	SMOreg	MP	MB
Correlation coefficient	0.93	0.93	0.7	0.75	0.88	0.9
Mean absolute error	0.06	0.6	0.14	0.13	0.085	0.07
Root mean squared error	0.085	0.088	0.17	0.16	0.11	0.1
Relative absolute error	28.62%	29.07%	68.70%	61.8%	41.01%	36.92%
Root relative squared error	36.2%	37.33%	71.52%	68.01%	47.07%	43.83%
Formula	Eq. S1	____	Eq. S2	Eq. S3	Eq. S4	____

According to Table 6, J_{SC} is predicted efficiently (R > 0.98) with all RT, RF, MB, and MP measures. Therefore, based on Tables 5 and 6, it can be found that by applying the machine learning computations, a valid model is developed for predicting experimental parameters to reduce these systems' operation and supervision costs.

Table 6. Performance of different algorithms due to prediction of J_{SC}

Statistical parameters	RT	RF	GP	SMOreg	MP	MB
Correlation coefficient	0.99	0.99	0.75	0.78	0.99	0.98
Mean absolute error	0.38	0.2	2.3	2.2	0.15	0.48
Root mean squared error	0.6	0.34	2.8	2.77	0.2	0.82
Relative absolute error	10.38%	5.52%	61.59%	58.71%	4.15%	12.91%
Root relative squared error	13.77%	7.82%	65.28%	63.36%	4.68%	18.94%
Formula	Eq. S5	____	Eq. S6	Eq. S7	Eq. S8	____

4. Conclusions

To obtain high efficiency in DSSCs, we synthesized GO-VI/TBP cobalt complex and employed it as an effective additive in sustainable electrolytes based on BMII and EMII ILs. With a simulated solar light illumination of AM 1.5, adding the ideal amount of 0.6 wt.% of this effective additive to the electrolyte considerably improved the electrochemical characteristics of DSSCs and demonstrated a conversion efficiency of 7.359%. The considerable influence of the presence of GO-VI/TBP cobalt complex in the electrolyte structure is shown by a 78.18% improvement in the efficiency of DSSCs with nanocomposite electrolytes compared to DSSCs with standard electrolyte. By adding cobalt complexes, pyridine, and imidazole compounds to the efficient additive structure of the GO-VI/TBP cobalt complex, the performance of DSSCs is greatly enhanced. This improvement is because cobalt and nitrogen-containing heterocyclic compounds can speed up electron transfer by accelerating redox pair (I^-/I_3^-) reactions and increasing the conductivity of the electrolyte. DFT calculations showed the quick penetration of electrons from the dye LUMO to the conduction band of the TiO_2 electrode through GO-VI/TBP cobalt complex adsorption because of the upward shift of the TiO_2's conduction band. Also, according to machine learning results, artificial intelligence methods are useful in predicting experimental values as they showed a statistical correlation above 0.93 with the actual observations. Hence, GO-VI/TBP cobalt complex can be used as an efficiency-enhancing factor in the fabrication of DSSCs and as an effective additive in the structure of ILs-based electrolytes.

References

[1] B. O'regan, M. Grätzel, A low-cost, high-efficiency solar cell based on dye-sensitized colloidal TiO2 films, nature 353 (1991) 737-740.

[2] S. Sharma, B. Siwach, S. Ghoshal, D. Mohan, Dye sensitized solar cells: From genesis to recent drifts, Renewable and Sustainable Energy Reviews 70 (2017) 529-537.

[3] P. Baskaran, K. Nisha, S. Harish, H. Ikeda, J. Archana, M. Navaneethan, Enhanced catalytic performance of Cu2ZnSnS4/MoS2 nanocomposites based counter electrode for Pt-free dye-sensitized solar cells, Journal of Alloys and Compounds 894 (2022) 162166.

[4] A.S. Mary, K. Bhojanaa, P. Murugan, A. Pandikumar, Experimental and theoretical study on optimizing CaxBa1− xSnO3 perovskite materials as photoanode of dye-sensitized solar cells, Journal of alloys and compounds 888 (2021) 161439.

[5] Y. Ren, D. Zhang, J. Suo, Y. Cao, F.T. Eickemeyer, N. Vlachopoulos, S.M. Zakeeruddin, A. Hagfeldt, M. Grätzel, Hydroxamic acid preadsorption raises efficiency of cosensitized solar cells, Nature (2022) 1-3.

[6] P.T. Nguyen, T.-D.T. Nguyen, V.S. Nguyen, D.T.-X. Dang, H.M. Le, T.-C. Wei, P.H. Tran, Application of deep eutectic solvent from phenol and choline chloride in electrolyte to improve stability performance in dye-sensitized solar cells, Journal of Molecular Liquids 277 (2019) 157-162.

[7] N.I.M.F. Hilmy, W.Z.N. Yahya, K.A. Kurnia, Eutectic ionic liquids as potential electrolytes in dye-sensitized solar cells: Physicochemical and conductivity studies, Journal of Molecular Liquids 320 (2020) 114381.

[8] N.I.M.F. Hilmy, W.Z.N. Yahya, S.N.A. Zaine, N.M. Mohamed, Photovoltaic performance of eutectic ionic liquids as potential electrolytes in dye-sensitized solar cells, Materials Today: Proceedings (2022).

[9] G. Kaur, H. Kumar, M. Singla, Diverse applications of ionic liquids: A comprehensive review, Journal of Molecular Liquids (2022) 118556.

[10] R. Kawano, H. Matsui, C. Matsuyama, A. Sato, M.A.B.H. Susan, N. Tanabe, M. Watanabe, High performance dye-sensitized solar cells using ionic liquids as their electrolytes, Journal of Photochemistry and Photobiology A: Chemistry 164 (2004) 87-92.

[11] R.A. Abu Talip, W.Z.N. Yahya, M.A. Bustam, Ionic Liquids Roles and Perspectives in Electrolyte for Dye-Sensitized Solar Cells, Sustainability 12 (2020) 7598.

[12] A.K. Bharwal, L. Manceriu, C. Olivier, A. Mahmoud, C. Iojoiu, T. Toupance, C.M. Ruiz, M. Pasquinelli, D. Duché, J.-J. Simon, Remarkable 8.3% efficiency and extended electron lifetime towards highly stable semi-transparent iodine-free DSSCs by mitigating the in-situ triiodide generation, Chemical Engineering Journal 446 (2022) 136777.

[13] B. Lin, H. Shang, F. Chu, Y. Ren, N. Yuan, B. Jia, S. Zhang, X. Yu, Y. Wei, J. Ding, Ionic liquid-tethered graphene oxide/ionic liquid electrolytes for highly efficient dye sensitized solar cells, Electrochimica Acta 134 (2014) 209-214.

[14] S. Venkatesan, E. Surya Darlim, M.-H. Tsai, H. Teng, Y.-L. Lee, Graphene oxide sponge as nanofillers in printable electrolytes in high-performance quasi-solid-state dye-sensitized solar cells, ACS applied materials & interfaces 10 (2018) 10955-10964.

[15] D.V. Raj, M. Balu, G. Baiju, G. Nagarajan, M.R. Subramaniam, D. Kumaresan, Fabrication of Cost-Effective Reduced Graphene Oxide Based Parallel Grids Embedded Dye-Sensitized Solar Mini-Modules, IEEE Journal of Photovoltaics 10 (2020) 1015-1022.

[16] H. Cai, J. Li, X. Xu, H. Tang, J. Luo, K. Binnemans, J. Fransaer, D.E. De Vos, Nanostructured composites of one-dimensional TiO2 and reduced graphene oxide for efficient dye-sensitized solar cells, Journal of Alloys and Compounds 697 (2017) 132-137.

[17] M.F.S.A. Razak, A. Badri, W.I. Nawawi, N. Sabani, M.K.A. Wahab, A.A. Shukor, Graphene-modified TiO2 as photoanode using agarose gel electrolyte for dye-sensitized solar cell, AIP Conference Proceedings, AIP Publishing LLC, 2022, pp. 020004.

[18] L.J. Brennan, S.T. Barwich, A. Satti, A. Faure, Y.K. Gun'ko, Graphene–ionic liquid electrolytes for dye sensitised solar cells, Journal of Materials Chemistry A 1 (2013) 8379-8384.

[19] K. Surana, S. Konwar, P.K. Singh, B. Bhattacharya, Utilizing reduced graphene oxide for achieving better efficient dye sensitized solar cells, Journal of Alloys and Compounds 788 (2019) 672-676.

[20] R. Aliakbari, E. Kowsari, H.R. Naderi, S. Ramakrishna, A. Chinnappan, M.D. Najafi, N-heterocycle-functionalized graphene oxide complexed with cobalt (II) as symmetric supercapacitor electrodes, Journal of Alloys and Compounds (2022) 165371.

[21] A.G. Kuba, Y.Y. Smolin, M. Soroush, K.K. Lau, Synthesis and integration of poly (1-vinylimidazole) polymer electrolyte in dye sensitized solar cells by initiated chemical vapor deposition, Chemical Engineering Science 154 (2016) 136-142.

[22] M.R. Chirani, E. Kowsari, H. SalarAmoli, M. Yousefzadeh, A. Chinnappan, S. Ramakrishna, Covalently functionalized graphene oxide with cobalt–nitrogen-enriched complex containing iodide ligand as charge carrier nanofiller for eco-friendly high performance ionic liquid-based dye-sensitized solar cell, Journal of Molecular Liquids 325 (2021) 115198.

[23] D. Xu, H. Zhang, X. Chen, F. Yan, Imidazolium functionalized cobalt tris (bipyridyl) complex redox shuttles for high efficiency ionic liquid electrolyte dye-sensitized solar cells, Journal of Materials Chemistry A 1 (2013) 11933-11941.

[24] L. Giribabu, R. Bolligarla, M. Panigrahi, Recent Advances of Cobalt (II/III) Redox Couples for Dye-Sensitized Solar Cell Applications, The Chemical Record 15 (2015) 760-788.

[25] K.-W. Lee, M. Kim, J.-M. Kim, J.J. Kim, I.-H. Lee, Enhanced photovoltaic performance of back-illuminated dye-sensitized solar cell based on TiO2 nanoparticle/nanowire composite film in cobalt redox system, Journal of Alloys and Compounds 656 (2016) 568-572.

[26] E. Kowsari, M.R. Chirani, High efficiency dye-sensitized solar cells with tetra alkyl ammonium cation-based ionic liquid functionalized graphene oxide as a novel additive in nanocomposite electrolyte, Carbon 118 (2017) 384-392.

[27] I. Ahmad, R. Jafer, S.M. Abbas, N. Ahmad, J. Iqbal, S. Bashir, A.A. Melaibari, M.H. Khan, Improving energy harvesting efficiency of dye sensitized solar cell by using cobalt-rGO co-doped TiO2 photoanode, Journal of Alloys and Compounds 891 (2022) 162040.

[28] Y. Yang, Z. Zhang, J. Gao, D. Pan, B. Yuan, X. Guo, G. Huang, Metal-organic materials as efficient additives in polymer electrolytes for quasi-solid-state dye-sensitized solar cells, Journal of Alloys and Compounds 726 (2017) 1286-1294.

[29] M.U. Rahman, F. Xie, Y. Li, X. Sun, M. Wei, Grafting cobalt sulfide on graphene nanosheets as a counterelectrode for dye-sensitized solar cells, Journal of Alloys and Compounds 808 (2019) 151701.

[30] S. Wang, M. Sina, P. Parikh, T. Uekert, B. Shahbazian, A. Devaraj, Y.S. Meng, Role of 4-tert-butylpyridine as a hole transport layer morphological controller in perovskite solar cells, Nano letters 16 (2016) 5594-5600.

[31] T.M. Koh, K. Nonomura, N. Mathews, A. Hagfeldt, M. Grätzel, S.G. Mhaisalkar, A.C. Grimsdale, Influence of 4-tert-butylpyridine in DSCs with CoII/III redox mediator, The Journal of Physical Chemistry C 117 (2013) 15515-15522.

[32] E. Marchini, S. Caramori, R. Boaretto, V. Cristino, R. Argazzi, A. Niorettini, C.A. Bignozzi, Self-Assembled Multinuclear Complexes for Cobalt (II/III) Mediated Sensitized Solar Cells, Applied Sciences 11 (2021) 2769.

[33] M.R. Chirani, E. Kowsari, S. Ramakrishna, H.S. Amoli, M. Yousefzadeh, 'A sustainable gel-state ionic liquid-based dye-sensitized solar cell with a novel synthesized lansoprazole functionalized graphene oxide, Journal of Molecular Liquids (2022) 119999.

[34] J. Wen, Z. Sun, Y. Qiao, Y. Zhou, Y. Liu, Q. Zhang, Y. Liu, S. Jiao, Ti3C2 MXene-Reduced Graphene Oxide Composite Polymer-Based Printable Electrolyte for Quasi-Solid-State Dye-Sensitized Solar Cells, ACS Applied Energy Materials 5 (2022) 3329-3338.

[35] T.-Y. Cho, S.-G. Yoon, S. Sekhon, C.-H. Han, Effect of Ionic Liquids with Different Cations in I-/I 3-Redox Electrolyte on the Performance of Dye-sensitized Solar Cells, Bulletin of the Korean Chemical Society 32 (2011) 2058-2062.

[36] S. William, J. Hummers, R.E. Offeman, Preparation of graphitic oxide, J. Am. Chem. Soc 80 (1958) 1339-1339.

[37] F. Shoushtarian, M.R.A. Moghaddam, E. Kowsari, Efficient regeneration/reuse of graphene oxide as a nanoadsorbent for removing basic Red 46 from aqueous solutions, Journal of Molecular Liquids 312 (2020) 113386.

[38] P. Makal, D. Das, Reduced Graphene Oxide-Laminated One-Dimensional TiO2–Bronze Nanowire Composite: An Efficient Photoanode Material for Dye-Sensitized Solar Cells, ACS omega 6 (2021) 4362-4373.

[39] M.A. Eshlaghi, E. Kowsari, A. Ehsani, B. Akbari-Adergani, M. Hekmati, Functionalized graphene oxide GO-[imi-(CH2) 2-NH2] as a high efficient material for electrochemical sensing of lead: Synthesis surface and electrochemical characterization, Journal of Electroanalytical Chemistry 858 (2020) 113784.

[40] S.K. Eshkalak, M. Khatibzadeh, E. Kowsari, A. Chinnappan, S. Ramakrishna, New functionalizaed graphene oxide based on a cobalt complex for black electrophoretic ink applications, Journal of Materials Chemistry C 6 (2018) 8726-8732.

[41] M. Mohamadi, E. Kowsari, V. Haddadi-Asl, M. Yousefzadeh, Fabrication, characterization and electromagnetic wave absorption properties of covalently modified reduced graphene oxide based on dinuclear cobalt complex, Composites Part B: Engineering 162 (2019) 569-579.

[42] C.-H. Tsai, C.-J. Shih, W.-S. Wang, W.-F. Chi, W.-C. Huang, Y.-C. Hu, Y.-H. Yu, Fabrication of reduced graphene oxide/macrocyclic cobalt complex nanocomposites as counter electrodes for Pt-free dye-sensitized solar cells, Applied Surface Science 434 (2018) 412-422.

[43] K. Subramani, S. Kowsik, M. Sathish, Facile and scalable ultra–fine cobalt oxide/reduced graphene oxide nanocomposites for high energy asymmetric supercapacitors, ChemistrySelect 1 (2016) 3455-3467.

[44] M. Govindasamy, S. Sakthinathan, S.M. Chen, T.W. Chiu, A. Sathiyan, J.P. Merlin, Reduced graphene oxide supported cobalt Bipyridyl complex for sensitive detection of methyl parathion in fruits and vegetables, Electroanalysis 29 (2017) 1950-1960.

[45] A.A. Ensafi, M. Jafari-Asl, B. Rezaei, Pyridine-functionalized graphene oxide, an efficient metal free electrocatalyst for oxygen reduction reaction, Electrochimica Acta 194 (2016) 95-103.

[46] A. Pourjavadi, N. Safaie, S.H. Hosseini, C. Bennett, Graphene oxide/poly (vinyl imidazole) nanocomposite: an effective support for preparation of highly loaded heterogeneous copper catalyst, Applied Organometallic Chemistry 29 (2015) 601-607.

[47] N. Seifvand, E. Kowsari, Novel TiO 2/graphene oxide functionalized with a cobalt complex for significant degradation of NO x and CO, RSC advances 5 (2015) 93706-93716.

[48] S. Rani, M. Kumar, R. Garg, S. Sharma, D. Kumar, Amide functionalized graphene oxide thin films for hydrogen sulfide gas sensing applications, IEEE Sensors Journal 16 (2016) 2929-2934.

[49] F.B. Ajdari, E. Kowsari, A. Ehsani, L. Chepyga, M. Schirowski, S. Jäger, O. Kasian, F. Hauke, T. Ameri, Melamine-functionalized graphene oxide: synthesis, characterization and considering as pseudocapacitor electrode material with intermixed POAP polymer, Applied Surface Science 459 (2018) 874-883.

[50] J. Choi, D.A. Reddy, M.J. Islam, R. Ma, T.K. Kim, Self-assembly of CeO2 nanostructures/reduced graphene oxide composite aerogels for efficient photocatalytic degradation of organic pollutants in water, Journal of Alloys and Compounds 688 (2016) 527-536.

[51] P.K. Kipkemboi, P.C. Kiprono, J.J. Sanga, Vibrational spectra of t-butyl alcohol, t-butylamine and t-butyl alcohol+ t-butylamine binary liquid mixtures, Bulletin of the Chemical Society of Ethiopia 17 (2003).

[52] F.T. Johra, J.-W. Lee, W.-G. Jung, Facile and safe graphene preparation on solution based platform, Journal of Industrial and Engineering Chemistry 20 (2014) 2883-2887.

[53] J. Wang, Z. Chen, B. Chen, Adsorption of polycyclic aromatic hydrocarbons by graphene and graphene oxide nanosheets, Environmental science & technology 48 (2014) 4817-4825.

[54] N.N. Taheri, B. Ramezanzadeh, M. Mahdavian, Application of layer-by-layer assembled graphene oxide nanosheets/polyaniline/zinc cations for construction of an effective epoxy coating anti-corrosion system, Journal of Alloys and Compounds 800 (2019) 532-549.

[55] Y. Kumar, A. Sharma, M.A. Ahmed, S.S. Mali, C.K. Hong, P.M. Shirage, Morphology-controlled synthesis and enhanced energy product (BH) max of CoFe 2 O 4 nanoparticles, New Journal of Chemistry 42 (2018) 15793-15802.

[56] L. Chen, D. Ding, C. Liu, H. Cai, Y. Qu, S. Yang, Y. Gao, T. Cai, Degradation of norfloxacin by CoFe2O4-GO composite coupled with peroxymonosulfate: a comparative study and mechanistic consideration, Chemical Engineering Journal 334 (2018) 273-284.

[57] J. Tang, S. Yin, X. Liu, Z. Kan, X. Zhang, M. Jiang, F. Tao, F. Wang, C. Li, Thiol-yne click reaction mediated photoelectrochemical detection of multi-sulfhydryl compounds based on diacetylene functionalized conjugated polymer, Sensors and Actuators B: Chemical (2021) 130207.

[58] A. Piñeiro-García, S.M. Vega-Díaz, F. Tristán, D. Meneses-Rodríguez, G.J. Labrada-Delgado, V. Semetey, New insights in the chemical functionalization of graphene oxide by thiol-ene Michael addition reaction, FlatChem 26 (2021) 100230.

[59] C.V. Pham, M. Eck, M. Krueger, Thiol functionalized reduced graphene oxide as a base material for novel graphene-nanoparticle hybrid composites, Chemical engineering journal 231 (2013) 146-154.

[60] R. Li, S. Yamashita, H. Kita, Investigating the chemical bonding state of graphite powder treated with magnesium (II) phosphate through EELS, TEM, and XPS analysis, Diamond and Related Materials 116 (2021) 108423.

[61] K. Xu, M. Zhou, W. Chen, Y. Zhu, X. Wang, Y. Zhang, Q. Zhang, Bioinspired polydopamine/graphene oxide/collagen nanofilms as a controlled release carrier of bioactive substances, Chemical Engineering Journal 405 (2021) 126930.

[62] M. Mohamadi, E. Kowsari, M. Yousefzadeh, A. Chinnappan, S. Ramakrishna, Highly-efficient microwave absorptivity in reduced graphene oxide modified with PTA@ imidazolium based dicationic ionic liquid and fluorine atom, Composites Science and Technology 188 (2020) 107960.

[63] A.A. Ashtiani, E. Kowsari, V. Haddadi-Asl, M. Yousefi, A. Chinnappan, S. Ramakrishna, Synthesis of novel functionalized graphene oxide with incorporation pyrimidine group including cobalt-iodine bonds their nanocomposites with p-type conductive polymer as excellent pseudocapacitor electrode materials, Journal of Materials Science: Materials in Electronics 30 (2019) 18439-18451.

[64] R. Karthik, S. Thambidurai, Synthesis of cobalt doped ZnO/reduced graphene oxide nanorods as active material for heavy metal ions sensor and antibacterial activity, Journal of Alloys and Compounds 715 (2017) 254-265.

[65] P. Hohenberg, W. Kohn, Inhomogeneous electron gas, Physical review 136 (1964) B864.

[66] W. Kohn, L.J. Sham, Self-consistent equations including exchange and correlation effects, Physical review 140 (1965) A1133.

[67] G. Kresse, J. Furthmüller, Efficiency of ab-initio total energy calculations for metals and semiconductors using a plane-wave basis set, Computational materials science 6 (1996) 15-50.

[68] G. Kresse, J. Furthmüller, "Efficient iterative schemes for ab initio total-energy calculations using a plane-wave basis set," Phys. Rev. B, vol. 54, pp. 11169-11186, (1996).

[69] J. Perdew, K. Burke, M. Ernzerhof, Generalized Gradient Approximation Made Simple. 1996, 77, 3865-3868, erratum, Phys. Rev. Lett 78 (1996) 1396.

[70] J. Paier, R. Hirschl, M. Marsman, G. Kresse, The Perdew–Burke–Ernzerhof exchange-correlation functional applied to the G2-1 test set using a plane-wave basis set, The Journal of chemical physics 122 (2005) 234102.

[71] P.E. Blöchl, Projector augmented-wave method, Physical review B 50 (1994) 17953.

[72] S. Grimme, S. Ehrlich, L. Goerigk, Effect of the damping function in dispersion corrected density functional theory, Journal of computational chemistry 32 (2011) 1456-1465.

[73] H.J. Monkhorst, J.D. Pack, Special points for Brillouin-zone integrations, Physical review B 13 (1976) 5188.

[74] M. Lazzeri, A. Vittadini, A. Selloni, Structure and energetics of stoichiometric TiO 2 anatase surfaces, Physical Review B 63 (2001) 155409.

[75] Y. Jiao, F. Zhang, M. Grätzel, S. Meng, Structure–Property Relations in All-Organic Dye-Sensitized Solar Cells, Advanced Functional Materials 23 (2013) 424-429.

[76] H.G. Yang, C.H. Sun, S.Z. Qiao, J. Zou, G. Liu, S.C. Smith, H.M. Cheng, G.Q. Lu, Anatase TiO 2 single crystals with a large percentage of reactive facets, Nature 453 (2008) 638-641.

[77] J.K. Burdett, T. Hughbanks, G.J. Miller, J.W. Richardson Jr, J.V. Smith, Structural-electronic relationships in inorganic solids: powder neutron diffraction studies of the rutile and anatase polymorphs of titanium dioxide at 15 and 295 K, Journal of the American Chemical Society 109 (1987) 3639-3646.

[78] W. Orellana, D-π-A dye attached on TiO2 (101) and TiO2 (001) surfaces: Electron transfer properties from ab initio calculations, Solar Energy 216 (2021) 266-273.

[79] N. Martsinovich, D.R. Jones, A. Troisi, Electronic structure of TiO2 surfaces and effect of molecular adsorbates using different DFT implementations, The Journal of Physical Chemistry C 114 (2010) 22659-22670.

[80] T. Bessho, S.M. Zakeeruddin, C.Y. Yeh, E.W.G. Diau, M. Grätzel, Highly efficient mesoscopic dye-sensitized solar cells based on donor–acceptor-substituted porphyrins, Angewandte Chemie International Edition 49 (2010) 6646-6649.

[81] Z. Cui, L. Kang, L. Li, L. Wang, K. Wang, A combined state-of-charge estimation method for lithium-ion battery using an improved BGRU network and UKF, Energy (2022) 124933.

[82] C. Liu, D. Li, L. Wang, L. Li, K. Wang, Strong robustness and high accuracy in predicting remaining useful life of supercapacitors, APL Materials 10 (2022) 061106.

[83] Z. Cui, J. Dai, J. Sun, D. Li, L. Wang, K. Wang, Hybrid methods using neural network and Kalman filter for the state of charge estimation of lithium-ion battery, Mathematical Problems in Engineering 2022 (2022).

[84] D. Li, L. Wang, C. Duan, Q. Li, K. Wang, Temperature prediction of lithium-ion batteries based on electrochemical impedance spectrum: A review, International Journal of Energy Research (2022).